Gradient-enhanced thermomechanical 3D model for simulation of transformation patterns in pseudoelastic shape memory alloys[⋆]

Mohsen Rezaee-Hajidehi[a], Karel Tůma[b], Stanisław Stupkiewicz[a,∗]

[a]*Institute of Fundamental Technological Research (IPPT), Polish Academy of Sciences,*
Pawińskiego 5B, 02-106 Warsaw, Poland
[b]*Faculty of Mathematics and Physics, Charles University, Sokolovskà 83, 186 75, Prague, Czech Republic*

Abstract

Stress-induced martensitic transformation in polycrystalline NiTi under tension often proceeds through formation and propagation of macroscopic phase transformation fronts, i.e., diffuse interfaces that separate the transformed and untransformed domains. A gradient-enhanced 3D finite-strain model of pseudoelasticity is developed in this work with the aim to describe the related phenomena. The underlying softening response is regularized by enhancing the Helmholtz free energy of a non-gradient model with a gradient term expressed in terms of the martensite volume fraction. To facilitate finite-element implementation, a micromorphic-type regularization is then introduced following the approach developed recently in the 1D small-strain context. The complete evolution problem is formulated within the incremental energy minimization framework, and the resulting non-smooth minimization problem is solved by employing the augmented Lagrangian technique. In order to account for the thermomechanical coupling effects, a general thermomechanical framework, which is consistent with the second law of thermodynamics and considers all related couplings, is also developed. Finite-element simulations of representative 3D problems show that the model is capable of representing the loading-rate effects in a NiTi dog-bone specimen and complex transformation patterns in a NiTi tube under tension. A parametric study is also carried out to investigate the effect of various parameters on the characteristics of the macroscopic transformation front.

Keywords: Phase transformation, Softening, Strain localization, Micromorphic regularization, Finite-element method

1. Introduction

Shape-memory alloys (SMAs) exhibit spectacular properties, for instance, the shape-memory effect and pseudoelasticity, which facilitates numerous advanced applications of this class of mate-

[∗]Corresponding author.
Email addresses: `mrezaee@ippt.pan.pl` (Mohsen Rezaee-Hajidehi), `ktuma@karlin.mff.cuni.cz` (Karel Tůma), `sstupkie@ippt.pan.pl` (Stanisław Stupkiewicz)

rials. The unique properties of SMAs result from the martensitic phase transformation that can be induced by varying the temperature or stress, and the related reversible strain due to the phase transformation or martensite variant rearrangement is the basic mechanism of inelastic deformation. The thermomechanical behaviour of SMAs is complex, and numerous models have been developed with the aim to describe the relevant effects at various scales, see, e.g., the review papers (Patoor et al., 2006; Lagoudas et al., 2006; Cissé et al., 2016).

One of the interesting features of polycrystalline SMAs is that the stress-induced transformation and the related deformation field are often nonuniform, even if the geometry and loading promote a uniform deformation. This, in particular, concerns polycrystalline NiTi under predominantly tensile loading (NiTi is commercially the most successful SMA, hence the importance of the related effects). The martensitic transformation proceeds then through formation and propagation of macroscopic transformation fronts, i.e., diffuse interfaces that separate transformed and untransformed domains.

In the case of NiTi strips under tension, the typical appearance of the macroscopic transformation fronts is in the form of planar interfaces that are inclined with respect to the loading axis (Shaw and Kyriakides, 1997; Pieczyska et al., 2006; Zhang et al., 2010; Kim and Daly, 2011) and the transformation pattern resembles then the Lüders bands characteristic, for instance, for low-carbon steels (Butler, 1962). Localized transformation is also observed in NiTi wires under tension (Churchill et al., 2009; Sedmák et al., 2016). Macroscopic transformation fronts of a more complex form, for instance, helical bands and multi-prong fronts, have been observed in NiTi tubes under uniaxial tension or under combined loading conditions (Sun and Li, 2002; Reedlunn et al., 2014; Bechle and Kyriakides, 2016). The transformation is nonuniform also in NiTi tubes under bending, in which diamond-like patterns are formed (Bechle and Kyriakides, 2014; Reedlunn et al., 2014).

In all cases mentioned above, the transformed and untransformed domains are separated by diffuse interfaces of finite thickness, which can be revealed by full-field measurements, e.g., by the digital image correlation (DIC) technique (Kim and Daly, 2011; Bechle and Kyriakides, 2014; Reedlunn et al., 2014) or by 3D synchrotron X-ray diffraction imaging (Sedmák et al., 2016). Two factors are expected to govern the interface thickness, namely the grain size and the specimen geometry, e.g., the tube thickness or the wire diameter. The related dependencies deserve more detailed experimental and theoretical studies, even if some related issues have already been discussed (e.g., He and Sun, 2009; Dong et al., 2016).

It is now agreed that the complex transformation patterns result from the intrinsic softening response, common for NiTi in tension. However, the softening response cannot be directly observed because it leads to strain localization, and the transformation proceeds then through propagation of macroscopic transformation fronts. The fronts propagate at an approximately constant load (in nearly isothermal conditions), so that the corresponding overall response of a specimen typically

exhibits a stress plateau. The overall specimen response is clearly distinct from and should not be confused with the intrinsic material response. This has been clearly demonstrated by Hallai and Kyriakides (2013) in the experiment in which the softening response of NiTi has been extracted from the overall response of a uniformly deforming laminate composed of NiTi and steel sheets, the latter of a known hardening elastoplastic response.

Modelling and simulation of strain localization and related transformation patterns is not straightforward because softening leads to ill-posedness of the corresponding boundary value problems. In computational practice, the difficulties are less severe than, for instance, in softening plasticity or damage, because the softening persists only in a bounded range of strains (typically of the order of several percent), and an apparent hardening is recovered after the transformation is completed. Accordingly, successful finite-element simulations of transformation patterning have been reported, which employ a local up-down-up material model with no additional regularization (Jiang et al., 2017a,b). This approach relies on a kind of natural regularization that results from the 3D effects, i.e., from the energy of elastic strains that ensure compatibility at macroscopic transformation fronts. However, the 3D effects do not fully regularize the problem, and the solution may depend on mesh size and mesh orientation, and the load–displacement response may exhibit spurious oscillations, see Mazière and Forest (2015). Furthermore, according to our experience, severe convergence problems may be encountered that spoil the robustness of the computational scheme. Note also that the regularizing 3D effects are lacking in 1D and 2D (plane stress) problems.

A possible remedy to the softening-related problems discussed above is to directly introduce the energy of macroscopic transformation fronts or, equivalently, a characteristic length-scale into the constitutive model. This can be achieved by enhancing the free energy with a higher-gradient term that represents the energy of the interface, typically expressed in terms of the strain gradient (Ren and Truskinovsky, 2000; Chang et al., 2006) or the gradient of the martensite volume fraction (Alessi and Bernardini, 2015; León Baldelli et al., 2015; Rezaee-Hajidehi and Stupkiewicz, 2018). The latter approach has also been adopted by Qiao et al. (2011) with the aim to model the size effects rather than transformation patterning. Note that the above models are restricted to the 1D setting. As a consequence of introducing the higher-gradient energy term, the transformation criterion becomes non-local in the sense that it involves, for instance, the Laplacian (i.e. the second spatial derivative) of the martensite volume fraction, and the computational treatment of the problem is then not immediate. In order to facilitate the finite-element implementation, a micromorphic-type regularization of the model has been introduced by Rezaee-Hajidehi and Stupkiewicz (2018), following the approach originally developed by Mazière and Forest (2015) for simulation of Lüders bands in plasticity, and this approach is further developed in this work in the 3D setting. A similar approach has been employed by Junker and Hackl (2014) to regularize their micromechanical model

of SMAs.

Another class of models relies on introducing a non-local counterpart of the martensite volume fraction that is governed by a Helmholtz-type partial differential equation, as in the so-called implicit gradient models of softening plasticity and damage (e.g., Peerlings et al., 1996). The non-local martensite volume fraction is then introduced directly into the transformation criterion (Duval et al., 2011; Armattoe et al., 2014; Badnava et al., 2014, 2018). The models of this type lack the variational structure of the models discussed earlier.

Transformation patterning has also been modelled using a phase-field type approach (He and Sun, 2010a; Wendler et al., 2017). In this approach, the volume fraction of martensite is governed by the evolution equation of the Ginzburg–Landau type, while the transformation strain of the martensite phase is prescribed and fixed, which is a restrictive assumption in the case of polycrystalline SMAs.

In this paper, the gradient-enhanced model developed by Rezaee-Hajidehi and Stupkiewicz (2018) in the 1D setting is extended to the 3D finite-strain setting. The distinctive features of the adopted approach include the incremental energy minimization framework and the micromorphic regularization of the gradient-enhanced model, which facilitates straightforward finite-element implementation of the model. The 3D finite-strain constitutive framework follows that developed by Stupkiewicz and Petryk (2013) with additional refinements concerning distinct elastic moduli of austenite and martensite and deformation-dependent hardening/softening response. Furthermore, the thermomechanical coupling is included in the model so that, in particular, the effect of the loading rate on the transformation pattern and overall response can be modelled in a physically sound manner (cf. Chang et al., 2006; Wendler et al., 2017; Badnava et al., 2018; Rezaee-Hajidehi and Stupkiewicz, 2018). A general thermomechanical formulation of the micromorphic model is thus developed that is consistent with the second law of thermodynamics and encompasses all possible couplings.

To show the capabilities of the model, three numerical examples are analyzed. The effect of the loading rate on the transformation pattern and pseudoelastic response of a NiTi dog-bone specimen under uniaxial tension is studied, and the results are compared to those obtained in the experiment (Zhang et al., 2010). Next, with reference to the experiment of Bechle and Kyriakides (2016), the complex transformation pattern in a NiTi tube under uniaxial tension is examined. Finally, a detailed study is carried out showing the effect of strip thickness, tension–compression asymmetry and transverse isotropy on the thickness and inclination angle of the macroscopic transformation front in a NiTi strip under uniaxial tension.

The paper is organized as follows. The gradient-enhanced model and its micromorphic regularization are introduced in Sections 2.1 and 2.2, respectively, and the governing equations that result

from the conditions of stationarity of the global incremental minimization problem are derived in Section 2.3. In Section 2.4, the model is extended by introducing the most essential thermomechanical couplings in a manner consistent with the general thermomechanical framework that is presented in Appendix B. Finite-element implementation of the model is discussed in Section 3, and numerical examples are reported in Section 4. The simplified case of the non-gradient 1D model is discussed in Appendix A as an illustration of the present constitutive framework.

2. Finite-strain model of pseudoelasticity

The gradient-enhanced model presented in this section is a generalization of the non-gradient finite-strain model of pseudoelasticity of Stupkiewicz and Petryk (2013). The gradient enhancement and its micromorphic regularization are introduced in Sections 2.1 and 2.2, respectively, following the approach developed by Rezaee-Hajidehi and Stupkiewicz (2018). Secondly, the most essential thermomechanical couplings are introduced in Section 2.4 in a manner consistent with the general framework presented in Appendix B. Additionally, the constitutive description is refined so that distinct elastic moduli of austenite and martensite are accounted for, as well as the deformation-dependent hardening/softening response, Section 2.1.1.

2.1. Gradient-enhanced model

The deformation gradient $\boldsymbol{F} = \nabla\boldsymbol{\varphi}$, where $\boldsymbol{\varphi}$ maps the material points from the reference configuration to the current configuration, $\boldsymbol{x} = \boldsymbol{\varphi}(\boldsymbol{X})$, and ∇ denotes the spatial gradient with respect to the reference configuration, is multiplicatively decomposed into its elastic part $\boldsymbol{F}^{\mathrm{e}}$ and transformation part $\boldsymbol{F}^{\mathrm{t}}$,

$$\boldsymbol{F} = \boldsymbol{F}^{\mathrm{e}}\boldsymbol{F}^{\mathrm{t}}. \tag{1}$$

The configuration of undeformed austenite is adopted as the reference configuration so that $\boldsymbol{F}^{\mathrm{t}} = \boldsymbol{I}$ in the fully austenitic state. Furthermore, it is assumed here that the martensitic transformation is isochoric so that $\boldsymbol{F}^{\mathrm{t}}$ satisfies the condition $\det \boldsymbol{F}^{\mathrm{t}} = 1$. This assumption can be easily relaxed, cf. Stupkiewicz and Petryk (2013), in order to account for the non-zero volume changes which are, however, typically very small.

The transformation deformation gradient $\boldsymbol{F}^{\mathrm{t}}$ admits the standard polar decomposition, $\boldsymbol{F}^{\mathrm{t}} = \boldsymbol{R}^{\mathrm{t}}\boldsymbol{U}^{\mathrm{t}}$, where $\boldsymbol{U}^{\mathrm{t}}$ is the (symmetric) transformation stretch tensor, and $\boldsymbol{R}^{\mathrm{t}}$ is the rotation tensor, $(\boldsymbol{R}^{\mathrm{t}})^{\mathrm{T}} = (\boldsymbol{R}^{\mathrm{t}})^{-1}$. Following Stupkiewicz and Petryk (2013), the transformation stretch $\boldsymbol{U}^{\mathrm{t}}$ is expressed in terms of the logarithmic transformation strain $\boldsymbol{e}^{\mathrm{t}}$, thus

$$\boldsymbol{U}^{\mathrm{t}} = \exp \boldsymbol{e}^{\mathrm{t}}, \tag{2}$$

5

where $\boldsymbol{e}^{\mathrm{t}}$ is a symmetric traceless tensor, $\operatorname{tr} \boldsymbol{e}^{\mathrm{t}} = 0$, so that the condition $\det \boldsymbol{F}^{\mathrm{t}} = \det \boldsymbol{U}^{\mathrm{t}} = 1$ is automatically satisfied in view of the standard property of the tensor exponential. If the material is elastically isotropic, the rotation tensor $\boldsymbol{R}^{\mathrm{t}}$ can be left unspecified as it does not enter the final constitutive equations, see below. Otherwise, $\boldsymbol{R}^{\mathrm{t}} = \boldsymbol{I}$ can be assumed thus leading to $\boldsymbol{F}^{\mathrm{t}} = \boldsymbol{U}^{\mathrm{t}}$.

The set $\mathcal{P}$ of admissible transformation strains, cf. Sadjadpour and Bhattacharya (2007), Stupkiewicz and Petryk (2013), is now defined in terms of the logarithmic transformation strain $\boldsymbol{e}^{\mathrm{t}}$,

$$\mathcal{P} = \{\boldsymbol{e}^{\mathrm{t}} \colon g(\boldsymbol{e}^{\mathrm{t}}) \leq 0\}, \tag{3}$$

where g is a function such that $g(\boldsymbol{0}) < 0$, $g(r\boldsymbol{e}^{\mathrm{t}})$ is a continuously increasing function of $r > 0$ for $\boldsymbol{e}^{\mathrm{t}} \neq \boldsymbol{0}$, and $g(\boldsymbol{e}^{\mathrm{t}}) = 0$ defines a smooth, closed and convex hypersurface in the deviatoric space. Features like tension–compression asymmetry and anisotropy due to crystallographic texture can be described by adequately specifying the constitutive function $g(\boldsymbol{e}^{\mathrm{t}})$, see Section 2.1.1.

Pseudoelasticity is associated with the stress-induced transformation in which the martensite variants are preferably oriented with respect to the applied stress. Accordingly, it is assumed that the martensite is *fully oriented* so that the transformation strain $\boldsymbol{e}^{\mathrm{t}}$ can be defined in terms of the volume fraction of martensite η and the transformation strain $\bar{\boldsymbol{e}}^{\mathrm{t}}$ of the fully oriented martensite, viz.

$$\boldsymbol{e}^{\mathrm{t}} = \eta \bar{\boldsymbol{e}}^{\mathrm{t}}, \qquad 0 \leq \eta \leq 1, \qquad \bar{\mathcal{P}} = \{\bar{\boldsymbol{e}}^{\mathrm{t}} \colon g(\bar{\boldsymbol{e}}^{\mathrm{t}}) = 0\}. \tag{4}$$

Here, $\bar{\mathcal{P}}$ is the set of limit transformation strains. Note that the volume fraction η is constrained between the physically-relevant limit values of $\eta = 0$ (pure austenite) and $\eta = 1$ (pure martensite). The split of $\boldsymbol{e}^{\mathrm{t}}$ into the product of η and $\bar{\boldsymbol{e}}^{\mathrm{t}}$ in Eq. (4) is unique for $\boldsymbol{e}^{\mathrm{t}} \neq \boldsymbol{0}$, while $\boldsymbol{e}^{\mathrm{t}} = \boldsymbol{0}$ corresponds to $\eta = 0$, $\bar{\boldsymbol{e}}^{\mathrm{t}}$ being indeterminate. Due to this indeterminacy, the case of $\eta \approx 0$ requires a special treatment in the computational scheme, as discussed in Section 3.2. For the same reason, the set $\bar{\mathcal{P}}$ has been defined by Stupkiewicz and Petryk (2013) such that the constraint on $\bar{\boldsymbol{e}}^{\mathrm{t}}$ is multiplied by η so that it is automatically satisfied for $\eta = 0$.

In the isothermal case, the Helmholtz free energy function (density per unit reference volume) is adopted in the following form,

$$\phi(\boldsymbol{F}, \bar{\boldsymbol{e}}^{\mathrm{t}}, \eta, \nabla\eta) = \phi_0(\eta) + \phi_{\mathrm{el}}(\boldsymbol{F}, \bar{\boldsymbol{e}}^{\mathrm{t}}, \eta) + \phi_{\mathrm{int}}(\bar{\boldsymbol{e}}^{\mathrm{t}}, \eta) + \phi_{\mathrm{grad}}(\nabla\eta), \tag{5}$$

where ϕ_0 represents the chemical energy contribution, ϕ_{el} is the elastic strain energy, ϕ_{int} is the internal interaction energy, and ϕ_{grad} is the gradient term. Upon eliminating the gradient term ϕ_{grad}, the local model of pseudoelasticity developed by Stupkiewicz and Petryk (2013) is recovered. The specific constitutive functions adopted for the individual free-energy contributions are provided later.

6

The global Helmholtz free energy functional Φ is defined as the integral over the body domain B in the reference configuration,

$$\Phi[\boldsymbol{\varphi}, \bar{\boldsymbol{e}}^{\mathrm{t}}, \eta] = \int_B \phi(\nabla\boldsymbol{\varphi}, \bar{\boldsymbol{e}}^{\mathrm{t}}, \eta, \nabla\eta)\mathrm{d}V, \tag{6}$$

and the functional of potential energy $\mathcal{E}$ is defined as

$$\mathcal{E}[\boldsymbol{\varphi}, \bar{\boldsymbol{e}}^{\mathrm{t}}, \eta] = \Phi[\boldsymbol{\varphi}, \bar{\boldsymbol{e}}^{\mathrm{t}}, \eta] + \Omega[\boldsymbol{\varphi}], \tag{7}$$

where Ω represents the potential of the external loads, which are assumed conservative. As an example, Ω is here defined in terms of the surface traction $\boldsymbol{t}^*$ prescribed on the boundary ∂B_t,

$$\Omega[\boldsymbol{\varphi}] = -\int_{\partial B_t} \boldsymbol{t}^* \cdot \boldsymbol{\varphi} \, \mathrm{d}S. \tag{8}$$

To complete the model, the rate-independent dissipation potential is defined in the following form

$$D(\dot{\eta}) = f_{\mathrm{c}}|\dot{\eta}|, \qquad f_{\mathrm{c}} > 0, \tag{9}$$

where f_{c} is the critical driving force. The dissipation potential (9) describes the dissipation due to forward ($\dot{\eta} > 0$) and reverse ($\dot{\eta} < 0$) transformation only. The dissipation associated with the evolution of $\bar{\boldsymbol{e}}^{\mathrm{t}}$, i.e. with reorientation of martensite, is not included in the model so that the model is more suitable for predominantly proportional loading–unloading paths.

The global dissipation potential is now formulated in the incremental form that corresponds to the typical time increment $t_n \to t_{n+1} = t_n + \Delta t$,

$$\Delta\mathcal{D}[\eta] = \int_B D(\eta - \eta_n)\mathrm{d}V, \tag{10}$$

where the local incremental potential $D(\Delta\eta) = f_{\mathrm{c}}|\Delta\eta|$ with $\Delta\eta = \eta - \eta_n$ results from the application of the backward-Euler integration scheme to the rate-potential (9). Here and in the following, the subscript n denotes the quantities corresponding to the previous time instant t_n, while the subscript $n+1$ indicating the quantities at the current time instant t_{n+1} is omitted for the sake of brevity.

Finally, the time-discrete evolution problem for the unknown fields of $\boldsymbol{\varphi}$, $\bar{\boldsymbol{e}}^{\mathrm{t}}$ and η at $t = t_{n+1}$ is formulated as the following incremental energy minimization problem (cf. Ortiz and Repetto, 1999; Petryk, 2003; Miehe, 2011; Stupkiewicz and Petryk, 2013; Rezaee-Hajidehi and Stupkiewicz, 2018; Tůma et al., 2018)

$$\{\boldsymbol{\varphi}, \bar{\boldsymbol{e}}^{\mathrm{t}}, \eta\} = \arg \min_{\boldsymbol{\varphi}, \bar{\boldsymbol{e}}^{\mathrm{t}}, \eta} \Pi[\boldsymbol{\varphi}, \bar{\boldsymbol{e}}^{\mathrm{t}}, \eta], \tag{11}$$

where the global incremental potential Π comprises the increments in the potential energy and dissipation, as well as the terms enforcing the constitutive constraints, viz.

$$\Pi[\boldsymbol{\varphi}, \bar{\boldsymbol{e}}^{\mathrm{t}}, \eta] = \mathcal{E}[\boldsymbol{\varphi}, \bar{\boldsymbol{e}}^{\mathrm{t}}, \eta] - \mathcal{E}[\boldsymbol{\varphi}_n, \bar{\boldsymbol{e}}_n^{\mathrm{t}}, \eta_n] + \Delta\mathcal{D}[\eta] + \mathcal{I}_{[0,1]}[\eta] + \mathcal{I}_{\bar{\mathcal{P}}}[\bar{\boldsymbol{e}}^{\mathrm{t}}]. \tag{12}$$

The term $\mathcal{I}_{[0,1]}[\eta]$ enforces the bound constraint on η through the indicator function $I_{[0,1]}(\eta)$,

$$\mathcal{I}_{[0,1]}[\eta] = \int_B I_{[0,1]}(\eta)\mathrm{d}V, \qquad I_{[0,1]}(\eta) = \begin{cases} 0 & \text{if } 0 \le \eta \le 1, \\ +\infty & \text{otherwise,} \end{cases} \tag{13}$$

and the term $\mathcal{I}_{\bar{\mathcal{P}}}[\bar{e}^\mathrm{t}]$ enforces $\bar{e}^\mathrm{t}$ to belong to the set $\bar{\mathcal{P}}$, cf. Eq. (4),

$$\mathcal{I}_{\bar{\mathcal{P}}}[\bar{e}^\mathrm{t}] = \int_B I_{\bar{\mathcal{P}}}(\bar{e}^\mathrm{t})\mathrm{d}V, \qquad I_{\bar{\mathcal{P}}}(\bar{e}^\mathrm{t}) = \begin{cases} 0 & \text{if } \bar{e}^\mathrm{t} \in \bar{\mathcal{P}}, \\ +\infty & \text{otherwise.} \end{cases} \tag{14}$$

2.1.1. The constitutive functions

The Helmholtz free energy function ϕ employed in this study, Eq. (5), is an extension of the one employed by Stupkiewicz and Petryk (2013) and includes some extra features. The individual components of ϕ are specified in the following.

The chemical energy contribution ϕ_0 is obtained as the weighted average of the free energy densities of pure austenite phase ϕ_0^a and pure martensite phase ϕ_0^m in a reference stress-free state, i.e.,

$$\phi_0(\eta) = (1 - \eta)\phi_0^\mathrm{a} + \eta\phi_0^\mathrm{m} = \phi_0^\mathrm{a} + \Delta\phi_0\eta, \tag{15}$$

where $\Delta\phi_0 = \phi_0^\mathrm{m} - \phi_0^\mathrm{a}$ is the chemical energy of transformation. The free energy density terms ϕ_0^a and ϕ_0^m, and thus also $\Delta\phi_0$, depend on the temperature. This dependence is not reflected here, as only the isothermal case is considered. The thermomechanical model is discussed in Section 2.4.

Assuming elastic isotropy, the elastic strain energy ϕ_el is adopted in the following neo-Hookean form,

$$\phi_\mathrm{el}(\boldsymbol{F}, \bar{e}^\mathrm{t}, \eta) = \frac{1}{2}\mu(\eta)(\operatorname{tr}\hat{\boldsymbol{b}}^\mathrm{e} - 3) + \frac{1}{4}\kappa(\det\boldsymbol{b}^\mathrm{e} - 1 - \log(\det\boldsymbol{b}^\mathrm{e})), \quad \hat{\boldsymbol{b}}^\mathrm{e} = (\det\boldsymbol{b}^\mathrm{e})^{-1/3}\boldsymbol{b}^\mathrm{e}, \tag{16}$$

where $\boldsymbol{b}^\mathrm{e}$ is the elastic left Cauchy–Green tensor,

$$\boldsymbol{b}^\mathrm{e} = \boldsymbol{F}^\mathrm{e}(\boldsymbol{F}^\mathrm{e})^\mathrm{T} = \boldsymbol{F}(\boldsymbol{C}^\mathrm{t})^{-1}\boldsymbol{F}^\mathrm{T}, \qquad \boldsymbol{C}^\mathrm{t} = (\boldsymbol{F}^\mathrm{t})^\mathrm{T}\boldsymbol{F}^\mathrm{t}, \tag{17}$$

and $\hat{\boldsymbol{b}}^\mathrm{e}$ is the volume-preserving part of $\boldsymbol{b}^\mathrm{e}$, $\det\hat{\boldsymbol{b}}^\mathrm{e} = 1$. In view of Eq. (2), we have $\boldsymbol{C}^\mathrm{t} = \exp(2e^\mathrm{t})$ and $(\boldsymbol{C}^\mathrm{t})^{-1} = \exp(-2e^\mathrm{t})$, so that $\boldsymbol{b}^\mathrm{e}$ is finally expressed as

$$\boldsymbol{b}^\mathrm{e} = \boldsymbol{F}\exp(-2\eta\bar{e}^\mathrm{t})\boldsymbol{F}^\mathrm{T}. \tag{18}$$

The shear modulus is here assumed different for the austenite and martensite phases, and in Eq. (16) it is thus a function of η, $\mu = \mu(\eta)$, while the bulk modulus $\kappa = \kappa_\mathrm{a} = \kappa_\mathrm{m}$ is assumed identical for both phases. Adopting the Voigt scheme (e.g. Auricchio et al., 2014; Cissé et al., 2017), the overall shear modulus μ is given by

$$\mu(\eta) = (1 - \eta)\mu_\mathrm{a} + \eta\mu_\mathrm{m}, \tag{19}$$

8

where μ_a and μ_m are, respectively, the shear moduli of the austenite and martensite phases. In this simple model, the shear modulus μ is the apparent modulus that may represent, in an approximate manner, also inelastic mechanisms such as the R-phase transformation in the austenitic state and detwinning in the martensitic state. Accordingly, the apparent moduli μ_a and μ_m may be significantly lower than the true elastic moduli of the respective phases. The related inelastic deformation mechanisms are approximately volume-preserving, and hence the bulk modulus is assumed constant.

The interaction energy ϕ_int is assumed in the following form,

$$\phi_\mathrm{int}(\bar{\boldsymbol{e}}^\mathrm{t}, \eta) = \frac{1}{2} H(\bar{\boldsymbol{e}}^\mathrm{t}) \eta^2, \tag{20}$$

where the state-dependent coefficient H controls the hardening/softening behaviour and is assumed to depend on the transformation strain $\bar{\boldsymbol{e}}^\mathrm{t}$ through the following function,

$$H(\bar{\boldsymbol{e}}^\mathrm{t}) = H_\mathrm{T} - \frac{(\epsilon_\mathrm{T} - \epsilon(\bar{\boldsymbol{e}}^\mathrm{t}))(H_\mathrm{T} - H_\mathrm{C})}{\epsilon_\mathrm{T} - \epsilon_\mathrm{C}}, \qquad \epsilon(\bar{\boldsymbol{e}}^\mathrm{t}) = \sqrt{\frac{2}{3} \operatorname{tr}(\bar{\boldsymbol{e}}^\mathrm{t})^2}, \tag{21}$$

where H_T and H_C are the hardening moduli corresponding to uniaxial tension and compression, respectively, and $\epsilon(\bar{\boldsymbol{e}}^\mathrm{t})$ is the equivalent strain. In uniaxial tension and compression, we have $\epsilon(\bar{\boldsymbol{e}}^\mathrm{t}) = \epsilon_\mathrm{T}$ and $\epsilon(\bar{\boldsymbol{e}}^\mathrm{t}) = \epsilon_\mathrm{C}$, respectively. The form (20) of the interaction energy is motivated by the frequent experimental evidence that NiTi exhibits softening in tension ($H_\mathrm{T} < 0$) and hardening in compression ($H_\mathrm{C} > 0$), while $\epsilon_\mathrm{T} > \epsilon_\mathrm{C}$.

Finally, the gradient term ϕ_grad is taken as

$$\phi_\mathrm{grad}(\nabla \eta) = \frac{1}{2} G \nabla \eta \cdot \nabla \eta, \tag{22}$$

where G is a positive parameter, and the gradient $\nabla \eta$ is determined with respect to the reference configuration. The gradient-enhancement could be alternatively formulated in the current configuration as the quadratic form of the spatial gradient of η. However, for relatively small strains, the difference is negligible, see Geers et al. (2003).

The gradient term ϕ_grad introduces energy associated with the gradient of the volume fraction η. In particular, in the case of a softening response (for $H < 0$), strain localization leads to formation of Lüders-like bands and macroscopic transformation fronts. The related high gradients of the volume fraction η are then penalized, and the gradient term ϕ_grad governs the energy of the macroscopic transformation fronts. As shown by Rezaee-Hajidehi and Stupkiewicz (2018), for a constant $H < 0$, parameter $G > 0$ defines a characteristic length $\lambda = \pi \sqrt{-G/H}$, which specifies the thickness of the diffuse interface (macroscopic transformation front). Therefore, a regularization is introduced by the present gradient enhancement to the otherwise ill-posed problem in the softening case $H < 0$. In the present model, the hardening/softening parameter $H(\bar{\boldsymbol{e}}^\mathrm{t})$ is no longer a constant, but the regularizing effect of the gradient term is similar.

A suitable function g that defines the set of admissible transformation strains is specified here by considering a transversely isotropic material with tension–compression asymmetry. Following the study of Sadjadpour and Bhattacharya (2007), see also Stupkiewicz and Petryk (2013), the function g is adopted as

$$g(\boldsymbol{e}^{\mathrm{t}}) = \left[(-I_2)^{3/2} - bI_3 - cI_4^3\right]^{1/3} - a, \tag{23}$$

where the invariants I_k are expressed as

$$I_2 = -\frac{1}{2}\operatorname{tr}(\boldsymbol{e}^{\mathrm{t}})^2, \qquad I_3 = \det \boldsymbol{e}^{\mathrm{t}}, \qquad I_4 = \boldsymbol{m} \cdot \boldsymbol{e}^{\mathrm{t}} \boldsymbol{m}, \tag{24}$$

with $\boldsymbol{m}$ as the axis of the rotational symmetry. Recall that $\boldsymbol{e}^{\mathrm{t}}$ is traceless, thus $I_1 = \operatorname{tr}\boldsymbol{e}^{\mathrm{t}} = 0$. In function g, the tension–compression asymmetry is controlled by parameter b, and transverse isotropy by parameter c. The case of $b = c = 0$ corresponds to an isotropic material with no tension–compression asymmetry.

The material parameters a, b and c in Eq. (23) can be expressed in terms of the transformation strains in uniaxial tension and compression along the symmetry axis $\boldsymbol{m}$ and in the perpendicular direction. Specifically,

$$a = \epsilon_{\mathrm{T}}\left[\frac{3\sqrt{3}}{4(1+\alpha^3)}\right]^{1/3}, \qquad b = \frac{\sqrt{3}}{6}\frac{9\alpha^3\beta^3 - 7\alpha^3 + 7\beta^3 - 9}{(1+\alpha^3)(1+\beta^3)}, \qquad c = \frac{2\sqrt{3}}{3}\frac{\alpha^3 - \beta^3}{(1+\alpha^3)(1+\beta^3)}, \tag{25}$$

where $\alpha = \epsilon_{\mathrm{T}}/\epsilon_{\mathrm{C}}$ and $\beta = \epsilon_{\mathrm{T}}^*/\epsilon_{\mathrm{C}}^*$, with ϵ_{T} and ϵ_{C} as, respectively, the maximum tensile and compressive strains along $\boldsymbol{m}$, and ϵ_{T}^* and ϵ_{C}^* as, respectively, the maximum tensile and compressive strains in the direction perpendicular to $\boldsymbol{m}$. In SMAs, the transformation strain is typically higher in tension than in compression, thus usually $\alpha > 1$ and $\beta > 1$, see e.g. Orgéas and Favier (1995).

To illustrate the constitutive response predicted by the present model, a simplified case of the non-gradient 1D small-strain model is discussed in Appendix A, see also Rezaee-Hajidehi and Stupkiewicz (2018). The predicted pseudoelastic response is sketched in Fig. 1(a). In the pseudoelastic range considered here, the typical stress-strain response consists of the initial elastic branch that corresponds to the elastic loading of pure austenite, followed by the transformation branch that exhibits hardening for $H > 0$ or softening for $H < 0$. The stress-induced transformation starts when the stress reaches the transformation stress, which is given by Eq. (A.6) in the 1D case discussed in Appendix A. In the case of softening, the boundary value problem is ill-posed, which is regularized here by the gradient term ϕ_{grad} in the free energy function (5). Once the transformation is completed ($\eta = 1$), further loading leads to elastic straining of pure martensite. Upon unloading, the reverse transformation proceeds once the respective transformation criterion is satisfied, cf. Eq. (A.6).
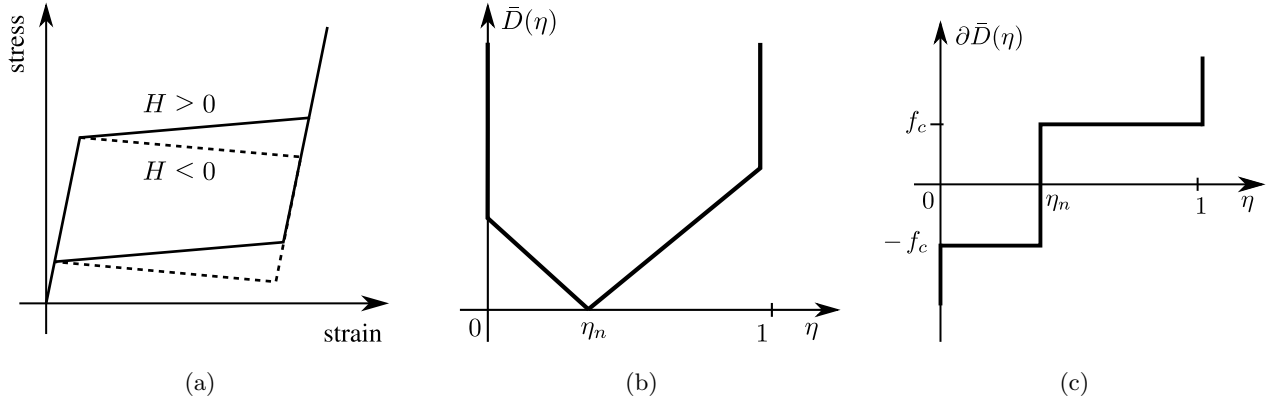
Figure 1: (a) Schematic of the pseudoelastic stress–strain response, (b) the graph of the non-smooth function $\bar{D}(\eta) = D(\eta - \eta_n) + I_{[0,1]}(\eta)$ and (c) its subdifferential $\partial \bar{D}(\eta)$.

2.2. Micromorphic regularization

Due to the presence of the Laplacian of η in the transformation criterion, see Rezaee-Hajidehi and Stupkiewicz (2018), it is not convenient to directly implement the gradient-enhanced model presented in Section 2.1. Accordingly, a micromorphic regularization of the model is performed here by introducing a micromorphic variable $\breve{\eta}$, which is the counterpart of the volume fraction of martensite η. For a comprehensive description of the micromorphic approach, the reader is referred to Forest (2016), see also Mazière and Forest (2015).

Referring to the original form (5), the Helmholtz free energy is now adopted as

$$\phi(\boldsymbol{F}, \bar{\boldsymbol{e}}^{\mathrm{t}}, \eta, \breve{\eta}, \nabla\breve{\eta}) = \phi_0(\eta) + \phi_{\mathrm{el}}(\boldsymbol{F}, \bar{\boldsymbol{e}}^{\mathrm{t}}, \eta) + \phi_{\mathrm{int}}(\bar{\boldsymbol{e}}^{\mathrm{t}}, \eta) + \phi_{\mathrm{grad}}(\eta, \breve{\eta}, \nabla\breve{\eta}), \tag{26}$$

where ϕ_{grad} is the gradient term that, upon the micromorphic regularization, takes the following form,

$$\phi_{\mathrm{grad}}(\eta, \breve{\eta}, \nabla\breve{\eta}) = \frac{1}{2}G\nabla\breve{\eta} \cdot \nabla\breve{\eta} + \frac{1}{2}\chi(\eta - \breve{\eta})^2. \tag{27}$$

The first term represents the gradient of the new global variable $\breve{\eta}$, and the second term enforces a penalization to the deviation of $\breve{\eta}$ from η, with $\chi > 0$ as a new model parameter. An indication on how to determine the value of parameter χ such that the deviation is sufficiently small can be found in Rezaee-Hajidehi and Stupkiewicz (2018), where the analytical solution is provided for the profile of the diffuse interface for the model with and without the micromorphic regularization.

In the micromorphic framework, the potential energy $\mathcal{E}$ is defined as,

$$\mathcal{E}[\boldsymbol{\varphi}, \bar{\boldsymbol{e}}^{\mathrm{t}}, \eta, \breve{\eta}] = \Phi[\boldsymbol{\varphi}, \bar{\boldsymbol{e}}^{\mathrm{t}}, \eta, \breve{\eta}] + \Omega[\boldsymbol{\varphi}], \qquad \Phi[\boldsymbol{\varphi}, \bar{\boldsymbol{e}}^{\mathrm{t}}, \eta, \breve{\eta}] = \int_B \phi(\nabla\boldsymbol{\varphi}, \bar{\boldsymbol{e}}^{\mathrm{t}}, \eta, \breve{\eta}, \nabla\breve{\eta})\mathrm{d}V, \tag{28}$$

and the time-discrete evolution problem with $\boldsymbol{\varphi}$, $\bar{\boldsymbol{e}}^{\mathrm{t}}$, η and $\breve{\eta}$ as the unknown fields is formulated as,

$$\{\boldsymbol{\varphi}, \bar{\boldsymbol{e}}^{\mathrm{t}}, \eta, \breve{\eta}\} = \arg \min_{\boldsymbol{\varphi}, \bar{\boldsymbol{e}}^{\mathrm{t}}, \eta, \breve{\eta}} \Pi[\boldsymbol{\varphi}, \bar{\boldsymbol{e}}^{\mathrm{t}}, \eta, \breve{\eta}], \tag{29}$$

11

where Π is the micromorphic incremental potential that, in analogy to Eq. (12), is defined as,

$$\Pi[\boldsymbol{\varphi}, \bar{\boldsymbol{e}}^{\mathrm{t}}, \eta, \breve{\eta}] = \mathcal{E}[\boldsymbol{\varphi}, \bar{\boldsymbol{e}}^{\mathrm{t}}, \eta, \breve{\eta}] - \mathcal{E}[\boldsymbol{\varphi}_n, \bar{\boldsymbol{e}}_n^{\mathrm{t}}, \eta_n, \breve{\eta}_n] + \Delta\mathcal{D}[\eta] + \mathcal{I}_{[0,1]}[\eta] + \mathcal{I}_{\bar{\mathcal{P}}}[\bar{\boldsymbol{e}}^{\mathrm{t}}]. \tag{30}$$

2.3. Stationarity conditions

In this section, we show that the conditions of stationarity of the micromorhpic incremental potential Π, Eq. (30), which are the necessary conditions for the minimum of Π in the minimization problem (29), yield the evolution equations for the internal variables $\bar{\boldsymbol{e}}^{\mathrm{t}}$ and η, as well as the global governing equations for $\boldsymbol{\varphi}$ and $\breve{\eta}$. The fields of $\bar{\boldsymbol{e}}^{\mathrm{t}}$ and η enter the micromorphic incremental potential Π through the free energy function ϕ, Eq. (26), that depends on $\bar{\boldsymbol{e}}^{\mathrm{t}}$ and η, but not on their gradients. Accordingly, minimization with respect to $\bar{\boldsymbol{e}}^{\mathrm{t}}$ and η can be performed locally (pointwise). Minimization with respect to $\boldsymbol{\varphi}$ and $\breve{\eta}$ must be performed globally because Π depends on the respective gradients.

The *pointwise* minimization problem for the local values of $\bar{\boldsymbol{e}}^{\mathrm{t}}$ and η is thus formulated as follows,

$$\{\bar{\boldsymbol{e}}^{\mathrm{t}}, \eta\} = \arg\min_{\bar{\boldsymbol{e}}^{\mathrm{t}}, \eta} \pi(\boldsymbol{F}, \bar{\boldsymbol{e}}^{\mathrm{t}}, \eta, \breve{\eta}, \nabla\breve{\eta}), \tag{31}$$

where the local incremental potential π takes the following form,

$$\pi(\boldsymbol{F}, \bar{\boldsymbol{e}}^{\mathrm{t}}, \eta, \breve{\eta}, \nabla\breve{\eta}) = \phi(\boldsymbol{F}, \bar{\boldsymbol{e}}^{\mathrm{t}}, \eta, \breve{\eta}, \nabla\breve{\eta}) - \phi(\boldsymbol{F}_n, \bar{\boldsymbol{e}}_n^{\mathrm{t}}, \eta_n, \breve{\eta}_n, \nabla\breve{\eta}_n) + D(\eta - \eta_n) + I_{[0,1]}(\eta) + I_{\bar{\mathcal{P}}}(\bar{\boldsymbol{e}}^{\mathrm{t}}), \tag{32}$$

so that $\Pi[\boldsymbol{\varphi}, \bar{\boldsymbol{e}}^{\mathrm{t}}, \eta, \breve{\eta}] = \int_B \pi(\nabla\boldsymbol{\varphi}, \bar{\boldsymbol{e}}^{\mathrm{t}}, \eta, \breve{\eta}, \nabla\breve{\eta})\mathrm{d}V$. The remaining arguments of π, i.e. $\{\boldsymbol{F}, \breve{\eta}, \nabla\breve{\eta}\}$, are the independent parameters in the minimization problem (31), and the solution $\{\bar{\boldsymbol{e}}^{\mathrm{t}}, \eta\}$ depends on $\{\boldsymbol{F}, \breve{\eta}, \nabla\breve{\eta}\}$.

Consider first the minimization of π with respect to η. It is apparent that the local incremental potential π is a non-smooth function of η in view of the terms $D(\eta - \eta_n)$ and $I_{[0,1]}(\eta)$. Following the approach of Rezaee-Hajidehi and Stupkiewicz (2018), see also Tůma et al. (2018), the necessary conditions for the minimum of π with respect to η can be written in the form of the following inclusion,

$$f_\eta \in \partial\bar{D}(\eta), \qquad \bar{D}(\eta) = D(\eta - \eta_n) + I_{[0,1]}(\eta), \tag{33}$$

where f_η is the thermodynamic driving force conjugate to η,

$$f_\eta = -\frac{\partial\phi}{\partial\eta}, \tag{34}$$

and $\bar{D}(\eta)$ is the non-smooth part of π, as illustrated in Fig. 1(b). The subdifferential $\partial\bar{D}(\eta)$, which is illustrated in Fig. 1(c), is a generalization of the derivative to non-smooth functions (Rockafellar, 1970; Morreau, 1974). In the computational treatment in Section 3, the non-smooth minimization problem (31) is transformed into an equivalent smooth saddle-point problem by using the augmented Lagrangian method, cf. Stupkiewicz and Petryk (2013).

12

It has been tacitly assumed here that π is convex in η so that the minimum exists and is unique. In the simple case of the 1D small-strain model, the condition for convexity in η can be easily derived, see Rezaee-Hajidehi and Stupkiewicz (2018). Specifically, the convexity is ensured if the softening modulus $H < 0$ is not excessively large in absolute value, namely $H > -E\epsilon_{\mathrm{T}}^2$, where E is the Young's modulus, and ϵ_{T} is the transformation strain. In practical terms, this condition is not restrictive and is satisfied for realistic values of model parameters. In the present case, the condition for convexity of π with respect to η is more involved, and thus it is not discussed here.

The minimization of the local incremental potential π with respect to $\bar{e}^{\mathrm{t}}$ can be performed by introducing a Lagrangian function L in which the equality constraint $g(\bar{e}^{\mathrm{t}}) = 0$, which enters π through the indicator function $I_{\bar{\mathcal{P}}}(\bar{e}^{\mathrm{t}})$, is introduced directly using the Lagrange multiplier ω, namely $L = \phi + \omega g(\bar{e}^{\mathrm{t}})$. Note that the free energy function ϕ included in L is the only remaining term in π that depends on $\bar{e}^{\mathrm{t}}$. The corresponding stationarity condition $\partial L/\partial \bar{e}^{\mathrm{t}} = \mathbf{0}$ yields then the following necessary condition for the minimum of π with respect to $\bar{e}^{\mathrm{t}}$,

$$\boldsymbol{f}_{\bar{e}^{\mathrm{t}}} = \omega \frac{\partial g(\bar{e}^{\mathrm{t}})}{\partial \bar{e}^{\mathrm{t}}}, \tag{35}$$

where $\boldsymbol{f}_{\bar{e}^{\mathrm{t}}}$ is the thermodynamic driving force conjugate to $\bar{e}^{\mathrm{t}}$,

$$\boldsymbol{f}_{\bar{e}^{\mathrm{t}}} = -\frac{\partial \phi}{\partial \bar{e}^{\mathrm{t}}}. \tag{36}$$

Accordingly, the condition (35) renders the driving force $\boldsymbol{f}_{\bar{e}^{\mathrm{t}}}$ normal to the surface of limit transformation strains $g(\bar{e}^{\mathrm{t}}) = 0$, see also Section 3.2.

Minimization with respect to the fields of $\boldsymbol{\varphi}$ and $\breve{\eta}$ is performed globally. The condition of stationarity of Π with respect to $\boldsymbol{\varphi}$ is

$$0 = \delta_{\boldsymbol{\varphi}}\Pi[\boldsymbol{\varphi}, \bar{e}^{\mathrm{t}}, \eta, \breve{\eta}] = \delta_{\boldsymbol{\varphi}}\mathcal{E}[\boldsymbol{\varphi}, \bar{e}^{\mathrm{t}}, \eta, \breve{\eta}] = \int_B \boldsymbol{P} \cdot \nabla\delta\boldsymbol{\varphi}\mathrm{d}V - \int_{\partial B_t} \boldsymbol{t}^* \cdot \delta\boldsymbol{\varphi}\mathrm{d}S \qquad \forall\,\delta\boldsymbol{\varphi}, \tag{37}$$

which is recognized as the virtual work principle, i.e. the weak form of the mechanical equilibrium, with $\delta\boldsymbol{\varphi}$ as the admissible virtual displacement satisfying $\delta\boldsymbol{\varphi} = \mathbf{0}$ on the boundary ∂B_{φ}, on which the Dirichlet boundary condition is prescribed for $\boldsymbol{\varphi}$, while $\boldsymbol{P}$ is the first Piola–Kirchhoff stress defined as,

$$\boldsymbol{P} = \frac{\partial \phi}{\partial \boldsymbol{F}}. \tag{38}$$

Following the standard procedure, the equilibrium equation in the strong form, along with the boundary condition on ∂B_t, are obtained from Eq. (37) in the following form,

$$\nabla \cdot \boldsymbol{P}^{\mathrm{T}} = \mathbf{0} \quad \text{in } B, \qquad \boldsymbol{P}\boldsymbol{\nu} = \boldsymbol{t}^* \quad \text{on } \partial B_t, \tag{39}$$

where $\nabla\cdot$ denotes the divergence operator in the reference configuration, thus $(\nabla\cdot\boldsymbol{P}^{\mathrm{T}})_i = \partial P_{ij}/\partial X_j$, and $\boldsymbol{\nu}$ is the unit outward normal to the boundary in the reference configuration.

Finally, the condition of stationarity of Π with respect to $\breve{\eta}$ is

$$0 = \delta_{\breve{\eta}}\Pi[\boldsymbol{\varphi}, \bar{\boldsymbol{e}}^{\mathrm{t}}, \eta, \breve{\eta}] = \delta_{\breve{\eta}}\mathcal{E}[\boldsymbol{\varphi}, \bar{\boldsymbol{e}}^{\mathrm{t}}, \eta, \breve{\eta}] = \int_B \big(G\nabla\breve{\eta} \cdot \nabla\delta\breve{\eta} - \chi(\eta - \breve{\eta})\delta\breve{\eta}\big)\mathrm{d}V \qquad \forall \delta\breve{\eta}. \qquad (40)$$

Again, following the standard procedure, the strong form of Eq. (40) is derived as

$$\breve{\eta} - \ell^2\nabla^2\breve{\eta} = \eta, \qquad \ell = \sqrt{\frac{G}{\chi}}, \qquad (41)$$

where ℓ is the internal length-scale parameter associated with the averaging operation delivered by Eq. (41). Assuming that the homogeneous Neumann boundary condition, $\nabla\breve{\eta} \cdot \boldsymbol{\nu} = 0$, holds on the entire boundary ∂B, Eq. (41) implies that $\int_B \eta\mathrm{d}V = \int_B \breve{\eta}\mathrm{d}V$.

The Helmholtz-type partial differential equation (41) is formally the same as the one employed for the regularization of damage or softening plasticity in the so-called implicit-gradient approach, cf. Peerlings et al. (1996). Here, it results in a natural way from the micromorphic approach, cf. Forest (2009), see also Mazière and Forest (2015).

The derived weak forms in Eqs. (37) and (40) form the basis for the finite-element implementation of the mechanical part of the problem with $\boldsymbol{\varphi}$ and $\breve{\eta}$ as the global unknowns. Minimization with respect to $\bar{\boldsymbol{e}}^{\mathrm{t}}$ and η can be performed locally, which is the beneficial feature of the micromorphic regularization introduced in Section 2.2. In the finite-element treatment, this leads to a nested iterative-subiterative scheme in which $\bar{\boldsymbol{e}}^{\mathrm{t}}$ and η are the local unknowns that are determined at the integration (Gauss) points, while $\boldsymbol{\varphi}$ and $\breve{\eta}$ are global unknowns. The computational treatment of the problem is discussed in Section 3.

2.4. Thermomechanically coupled model

In this section, a simple thermomechanically coupled model is introduced in which only two most essential thermomechanical couplings are accounted for. This model is utilized in the numerical examples presented in this paper, see Section 4. The model is a special case of the general model that includes all possible thermomechanical couplings, which is derived in Appendix B.

Firstly, the dependence of the chemical energy contribution ϕ_0 on the temperature T is introduced into the model,

$$\phi_0(\eta, T) = \phi_0^{\mathrm{a}}(T) + \Delta\phi_0(T)\eta, \qquad \Delta\phi_0(T) = \phi_0^{\mathrm{m}}(T) - \phi_0^{\mathrm{a}}(T), \qquad (42)$$

see Eq. (15). The free energy of each pure phase in a reference stress-free state is adopted in the following form (Raniecki et al., 1992; Helm, 2007),

$$\phi_0^{\alpha}(T) = u_0^{\alpha} - s_0^{\alpha}T + \varrho_0 c^{\alpha}\Big(T - T_0 - T\log\frac{T}{T_0}\Big), \qquad \alpha \in \{\mathrm{a}, \mathrm{m}\}, \qquad (43)$$

where the superscript α denotes austenite or martensite, u_0^{α} is the internal energy, s_0^{α} is the entropy, $\varrho_0 c^{\alpha}$ is the specific heat (assumed here temperature-independent), and T_0 is the reference

temperature. Recall that the free energy ϕ is here the density per unit volume in the reference configuration, and the reference configuration is that of the undeformed austenite. Accordingly, all the material parameters introduced above, including those that correspond to the martensite phase, are the densities per unit volume of austenite. In the general case, when the phase transformation does not preserve volume (i.e. $\det \boldsymbol{U}^{\mathrm{t}} \neq 1$), the parameters that correspond to the martensite phase $(u_0^{\mathrm{m}}, s_0^{\mathrm{m}}, c^{\mathrm{m}})$ are thus obtained by adequate scaling of the respective densities per unit volume of martensite. This is not the case here, as we assume that $\det \boldsymbol{U}^{\mathrm{t}} = 1$.

Assuming equal specific heat capacities of pure austenite and martensite phases, $c^{\mathrm{a}} = c^{\mathrm{m}} = c$, the chemical energy of transformation $\Delta\phi_0$ is obtained as a linear function of the temperature T,

$$\Delta\phi_0(T) = -\Delta u^* + \Delta s^* T = \Delta s^*(T - T_{\mathrm{t}}), \tag{44}$$

where $\Delta u^* = u_0^{\mathrm{a}} - u_0^{\mathrm{m}} > 0$, $\Delta s^* = s_0^{\mathrm{a}} - s_0^{\mathrm{m}} > 0$, and $T_{\mathrm{t}} = \Delta u^*/\Delta s^*$ is the transformation (equilibrium) temperature. The remaining contributions to the Helmholtz free energy (ϕ_{el}, ϕ_{int}, ϕ_{grad}) are here considered temperature-independent.

Secondly, the latent heat of transformation and the heat due to the intrinsic dissipation are introduced into the heat conduction equation as the internal heat source (per unit reference volume),

$$\dot{R} = \Delta s^* T \dot{\eta} + f_{\mathrm{c}}|\dot{\eta}|. \tag{45}$$

Here, the term $\Delta s^* T > 0$ is the latent heat of transformation, thus the first term of $\dot{R}$ is positive during the forward transformation ($\dot{\eta} > 0$) and negative during the reverse transformation ($\dot{\eta} < 0$).

The heat conduction equation is formulated in the reference configuration, cf. e.g. Holzapfel (2006),

$$\varrho_0 c \dot{T} + \nabla \cdot \boldsymbol{Q} = \dot{R}, \qquad \boldsymbol{Q} = J \boldsymbol{F}^{-1} \boldsymbol{q}, \tag{46}$$

where $\boldsymbol{Q}$ is the nominal heat flux, $\boldsymbol{q}$ is the Cauchy heat flux, and $J = \det \boldsymbol{F}$. For an isotropic material, the Fourier's law is formulated in the current configuration in terms of the Cauchy heat flux $\boldsymbol{q}$, or equivalently in the referential description employing the nominal heat flux $\boldsymbol{Q}$,

$$\boldsymbol{q} = -k\, \nabla_{\boldsymbol{x}} T, \qquad \boldsymbol{Q} = -K \boldsymbol{C}^{-1} \nabla T, \tag{47}$$

where $\nabla_{\boldsymbol{x}}$ denotes the gradient in the current configuration, $k > 0$ is the thermal conductivity coefficient, the transformation rule $K = Jk$ defines the thermal conductivity coefficient K relative to the reference configuration, and $\boldsymbol{C} = \boldsymbol{F}^{\mathrm{T}} \boldsymbol{F}$ is the right Cauchy–Green tensor. The heat conduction equation is accompanied by the following boundary conditions

$$T = T^* \quad \text{on } \partial B_T, \qquad \boldsymbol{Q}\boldsymbol{\nu} = Q_{\nu} \quad \text{on } \partial B_q, \tag{48}$$

where T^* is the temperature prescribed on the boundary ∂B_T, and Q_{ν} is the heat flux prescribed on the boundary ∂B_q. In the case of the convective boundary condition, the heat flux is given by

$Q_\nu = h(T - T_\infty)$, where $h > 0$ is the heat convection coefficient and T_∞ is the temperature of the surrounding.

Following the standard procedure, the weak form of the heat conduction problem specified by Eqs. (46)–(48) is obtained as

$$\int_B \left((\varrho_0 c \dot{T} - \dot{R})\delta T + K \nabla T \cdot \boldsymbol{C}^{-1} \nabla \delta T\right) \mathrm{d}V + \int_{\partial B_q} Q_\nu \delta T \mathrm{d}S = 0 \qquad \forall \, \delta T, \tag{49}$$

where the test function δT vanishes on ∂B_T. The time-discrete formulation is obtained by applying the backward-Euler scheme so that $\dot{T} = (T - T_n)/\Delta t$ and $\dot{R} = (\Delta s^* T(\eta - \eta_n) + f_\mathrm{c}|\eta - \eta_n|)/\Delta t$.

3. Finite-element implementation

3.1. Augmented Lagrangian treatment of the non-smooth minimization problem (31)

The main difficulty in the finite-element implementation of the minimization problem (31) is the non-differentiability of the term $\bar{D}(\eta) = D(\eta - \eta_n) + I_{[0,1]}(\eta)$ in the local incremental potential π, Eq. (32). Following Stupkiewicz and Petryk (2013), the augmented Lagrangian method is here employed so that the non-smooth minimization problem (31) is transformed to an equivalent smooth, unconstrained saddle-point problem

$$\{\bar{\boldsymbol{e}}^\mathrm{t}, \eta, \lambda, \omega\} = \arg \min_{\bar{\boldsymbol{e}}^\mathrm{t}, \eta} \max_{\lambda, \omega} \mathcal{L}(\boldsymbol{F}, T, \bar{\boldsymbol{e}}^\mathrm{t}, \eta, \breve{\eta}, \nabla \breve{\eta}, \lambda, \omega), \tag{50}$$

where λ^1 and ω are Lagrange multipliers, the Lagrange function $\mathcal{L}$ is defined as

$$\mathcal{L}(\boldsymbol{F}, T, \bar{\boldsymbol{e}}^\mathrm{t}, \eta, \breve{\eta}, \nabla \breve{\eta}, \lambda, \omega) = \phi(\boldsymbol{F}, T, \bar{\boldsymbol{e}}^\mathrm{t}, \eta, \breve{\eta}, \nabla \breve{\eta}) + l_\mathrm{t}(\eta, \lambda) + \omega \, \eta \, g(\bar{\boldsymbol{e}}^\mathrm{t}), \tag{51}$$

and l_t is a continuously differentiable function of η and λ that replaces the non-differentiable function $\bar{D}$ in π. The essential feature of the augmented Lagrangian treatment is that a single Lagrange multiplier λ is used to handle the non-smooth dissipation potential and to enforce the bound constraints $0 \leq \eta \leq 1$. For the details, the reader is referred to Stupkiewicz and Petryk (2013), see also Tůma et al. (2018). For the sake of conciseness, the expression for l_t is not provided here.

The last term in $\mathcal{L}$ in Eq. (51) enforces the equality constraint $g(\bar{\boldsymbol{e}}^\mathrm{t}) = 0$ using the usual Lagrange multiplier technique, where ω is the corresponding Lagrange multiplier. The constraint is multiplied by η in order to facilitate the adequate treatment of the case of $\eta \approx 0$, as explained in Section 3.2, see also Stupkiewicz and Petryk (2013).

The solution of the saddle-point problem (50) is found by solving the conditions of stationarity of $\mathcal{L}$ that are the necessary conditions for the minimum of π. Since the augmented Lagrangian (51) is smooth, the stationarity conditions

$$\mathbf{Q}(\boldsymbol{\mathcal{F}}, \mathbf{h}) = \mathbf{0}, \tag{52}$$

---

[1]Not to be confused with the diffuse interface thickness λ used in Sections 2.1.1 and 4.3.

where

$$\mathbf{Q}(\boldsymbol{\mathcal{F}}, \mathbf{h}) = \frac{\partial \mathcal{L}(\boldsymbol{\mathcal{F}}, \mathbf{h})}{\partial \mathbf{h}}, \qquad \boldsymbol{\mathcal{F}} = \{\boldsymbol{F}, T, \breve{\eta}, \nabla\breve{\eta}\}, \qquad \mathbf{h} = \{\bar{\boldsymbol{e}}^{\mathrm{t}}, \eta, \lambda, \omega\}, \tag{53}$$

can be solved directly at each integration point for the current local variables $\mathbf{h}$, while the current control variables $\boldsymbol{\mathcal{F}}$ are treated as known. The nonlinear equations (52) are solved in an iterative manner by using the Newton method. The implicit derivative of the solution $\mathbf{h}$ with respect to the control variables $\boldsymbol{\mathcal{F}}$, which is needed to obtain the consistent tangent in the complete iterative-subiterative scheme, is obtained in the standard manner, cf. Stupkiewicz and Petryk (2013), see also Michaleris et al. (1994) and Korelc (2009) for the general context.

3.2. Treatment of the case of $\eta \approx 0$

Consider the condition of stationarity of the Lagrangian $\mathcal{L}$ with respect to $\bar{\boldsymbol{e}}^{\mathrm{t}}$, viz.

$$\frac{\partial \mathcal{L}}{\partial \bar{\boldsymbol{e}}^{\mathrm{t}}} = \mathbf{0}, \qquad \frac{\partial \mathcal{L}}{\partial \bar{\boldsymbol{e}}^{\mathrm{t}}} = \frac{\partial \phi}{\partial \bar{\boldsymbol{e}}^{\mathrm{t}}} + \omega\eta\frac{\partial g(\bar{\boldsymbol{e}}^{\mathrm{t}})}{\partial \bar{\boldsymbol{e}}^{\mathrm{t}}} = -\boldsymbol{f}_{\bar{\boldsymbol{e}}^{\mathrm{t}}} + \omega\eta\frac{\partial g(\bar{\boldsymbol{e}}^{\mathrm{t}})}{\partial \bar{\boldsymbol{e}}^{\mathrm{t}}}, \tag{54}$$

where $\boldsymbol{f}_{\bar{\boldsymbol{e}}^{\mathrm{t}}}$ is the thermodynamic driving force conjugate to $\bar{\boldsymbol{e}}^{\mathrm{t}}$, cf. Eq. (36). We note that ϕ_{el} depends on $\bar{\boldsymbol{e}}^{\mathrm{t}}$ only through $\boldsymbol{e}^{\mathrm{t}} = \eta\bar{\boldsymbol{e}}^{\mathrm{t}}$, cf. Eqs. (16) and (18), and ϕ_{int} involves the term η^2. Accordingly, $\boldsymbol{f}_{\bar{\boldsymbol{e}}^{\mathrm{t}}}$ vanishes for $\eta = 0$, and the stationarity condition (54) is ill-posed for $\eta \approx 0$. Following Stupkiewicz and Petryk (2013), the stationarity condition (54) is equivalently written as

$$\frac{\partial \mathcal{L}}{\partial \bar{\boldsymbol{e}}^{\mathrm{t}}} = \eta\Big(\frac{\partial \phi}{\partial \boldsymbol{e}^{\mathrm{t}}} + \omega\frac{\partial g(\bar{\boldsymbol{e}}^{\mathrm{t}})}{\partial \bar{\boldsymbol{e}}^{\mathrm{t}}}\Big) = 0, \tag{55}$$

in view of $\boldsymbol{e}^{\mathrm{t}} = \eta\bar{\boldsymbol{e}}^{\mathrm{t}}$. The first term in the parentheses is now non-zero for a non-zero stress also when $\eta = 0$, which can be checked in a straightforward manner in the small-strain case, see Stupkiewicz and Petryk (2013), while the corresponding derivation is more involved in the finite-strain case, and it is thus omitted here. Accordingly, upon scaling by $1/\eta$, the stationarity condition (55) delivers a well-posed equation for $\bar{\boldsymbol{e}}^{\mathrm{t}}$ for arbitrary η. Note that the equality constraint $g(\bar{\boldsymbol{e}}^{\mathrm{t}}) = 0$ has been multiplied by η prior to introducing it to the Lagrangian $\mathcal{L}$ in Eq. (51), which facilitates the specific form (55) of the stationarity condition.

The vector $\mathbf{h}$ of local unknowns is now split,

$$\mathbf{h} = \{\mathbf{h}_1, \mathbf{h}_2\}, \qquad \mathbf{h}_1 = \{\bar{\boldsymbol{e}}^{\mathrm{t}}, \omega\}, \qquad \mathbf{h}_2 = \{\eta, \lambda\}, \tag{56}$$

and so is the local residual,

$$\hat{\mathbf{Q}}(\boldsymbol{\mathcal{F}}, \mathbf{h}) = \{\hat{\mathbf{Q}}_1, \mathbf{Q}_2\} = \mathbf{0}, \qquad \hat{\mathbf{Q}}_1 = \frac{1}{\eta}\frac{\partial \mathcal{L}}{\partial \mathbf{h}_1}, \qquad \mathbf{Q}_2 = \frac{\partial \mathcal{L}}{\partial \mathbf{h}_2}, \tag{57}$$

such that the part corresponding to $\mathbf{h}_1$ is scaled by $1/\eta$, as discussed above. Solution of the modified stationarity conditions $\hat{\mathbf{Q}} = \mathbf{0}$ proceeds then as described in Section 3.1.

17

3.3. Finite-element discretization

The complete thermomechanically coupled problem involves three unknown global fields ($\boldsymbol{\varphi}$, $\breve{\eta}$, T). The respective governing equations in weak form, Eqs. (37), (40) and (49), constitute the basis for the finite-element implementation, as briefly described below.

Let us write the virtual work principle (37) in the following compact form

$$\mathcal{G}_{\boldsymbol{\varphi}}[\boldsymbol{\varphi}, \delta\boldsymbol{\varphi}; \breve{\eta}, T] = 0 \qquad \forall\, \delta\boldsymbol{\varphi}, \tag{58}$$

in which $\breve{\eta}$ and T are included as additional arguments to indicate the coupling with the remaining global subproblems, while the dependence on the local variables $\bar{\boldsymbol{e}}^{\mathrm{t}}$ and η is not indicated. Likewise, the weak form (40) of the Helmholtz-type partial differential equation (41) is written as

$$\mathcal{G}_{\breve{\eta}}[\breve{\eta}, \delta\breve{\eta}; \boldsymbol{\varphi}, T] = 0 \qquad \forall\, \delta\breve{\eta}, \tag{59}$$

again with $\boldsymbol{\varphi}$ and T as the additional arguments indicating the respective couplings. Finally, upon the time discretization, the weak form (49) of the heat conduction equation is expressed as

$$\mathcal{G}_{T}[T, \delta T; \boldsymbol{\varphi}, \breve{\eta}] = 0 \qquad \forall\, \delta T, \tag{60}$$

with $\boldsymbol{\varphi}$ and $\breve{\eta}$ as the additional arguments.

The finite element approximation of the global fields of $\boldsymbol{\varphi}$, $\breve{\eta}$ and T is introduced in the standard manner,

$$\boldsymbol{\varphi}^{h} = \sum_{i} N_{i}^{(\boldsymbol{\varphi})} \boldsymbol{\varphi}_{i}, \qquad \breve{\eta}^{h} = \sum_{i} N_{i}^{(\breve{\eta})} \breve{\eta}_{i}, \qquad T^{h} = \sum_{i} N_{i}^{(T)} T_{i}, \tag{61}$$

where $\boldsymbol{\varphi}_{i}$, $\breve{\eta}_{i}$ and T_{i} denote the respective nodal values, and $N_{i}^{(\boldsymbol{\varphi})}$, $N_{i}^{(\breve{\eta})}$ and $N_{i}^{(T)}$ are the corresponding basis functions. In the present implementation, isoparametric hexahedral elements are used with triquadratic shape functions for the placement $\boldsymbol{\varphi}$ (i.e. 27 nodes per element), and with trilinear shape functions for the fields of $\breve{\eta}$ and T (i.e. 8 nodes per element).

Upon applying the Galerkin method, so that $\delta\boldsymbol{\varphi}^{h} = \sum_{i} N_{i}^{(\boldsymbol{\varphi})} \delta\boldsymbol{\varphi}_{i}$, etc., and substituting the finite-element approximation (61) into the weak forms (58)–(60), the discretized weak forms are obtained as

$$\mathcal{G}_{\boldsymbol{\varphi}}^{h}(\mathbf{U}, \delta\mathbf{U}; \mathbf{H}, \mathbf{T}) = \mathcal{G}_{\boldsymbol{\varphi}}[\boldsymbol{\varphi}^{h}, \delta\boldsymbol{\varphi}^{h}; \breve{\eta}^{h}, T^{h}] = 0 \qquad \forall\, \delta\mathbf{U}, \tag{62}$$

$$\mathcal{G}_{\breve{\eta}}^{h}(\mathbf{H}, \delta\mathbf{H}; \mathbf{U}, \mathbf{T}) = \mathcal{G}_{\breve{\eta}}[\breve{\eta}^{h}, \delta\breve{\eta}^{h}; \boldsymbol{\varphi}^{h}, T^{h}] = 0 \qquad \forall\, \delta\mathbf{H}, \tag{63}$$

$$\mathcal{G}_{T}^{h}(\mathbf{T}, \delta\mathbf{T}; \mathbf{U}, \mathbf{H}) = \mathcal{G}_{T}[T^{h}, \delta T^{h}; \boldsymbol{\varphi}^{h}, \breve{\eta}^{h}] = 0 \qquad \forall\, \delta\mathbf{T}, \tag{64}$$

where $\mathbf{U}$, $\mathbf{H}$ and $\mathbf{T}$ are the global vectors of nodal unknowns $\boldsymbol{u}_{i}$, $\breve{\eta}_{i}$ and T_{i}, respectively, where $\boldsymbol{u}_{i} = \boldsymbol{\varphi}_{i} - \boldsymbol{X}_{i}$ is the nodal displacement which is the actual unknown in the finite-element implementation.

Since $\mathcal{G}^h_{\boldsymbol{\varphi}}$, $\mathcal{G}^h_{\breve{\eta}}$ and $\mathcal{G}^h_T$ are linear in the variations $\delta\mathbf{U}$, $\delta\mathbf{H}$ and $\delta\mathbf{T}$, respectively, we have

$$\mathcal{G}^h_{\boldsymbol{\varphi}}(\mathbf{U}, \delta\mathbf{U}; \mathbf{H}, \mathbf{T}) = \mathbf{R}_{\boldsymbol{\varphi}}(\mathbf{U}; \mathbf{H}, \mathbf{T}) \cdot \delta\mathbf{U} = 0 \qquad \forall\, \delta\mathbf{U}, \tag{65}$$

$$\mathcal{G}^h_{\breve{\eta}}(\mathbf{H}, \delta\mathbf{H}; \mathbf{U}, \mathbf{T}) = \mathbf{R}_{\breve{\eta}}(\mathbf{H}; \mathbf{U}, \mathbf{T}) \cdot \delta\mathbf{H} = 0 \qquad \forall\, \delta\mathbf{H}, \tag{66}$$

$$\mathcal{G}^h_T(\mathbf{T}, \delta\mathbf{T}; \mathbf{U}, \mathbf{H}) = \mathbf{R}_T(\mathbf{T}; \mathbf{U}, \mathbf{H}) \cdot \delta\mathbf{T} = 0 \qquad \forall\, \delta\mathbf{T}, \tag{67}$$

which implies the following residual form of the discretized incremental governing equations,

$$\mathbf{R}_{\boldsymbol{\varphi}}(\mathbf{U}; \mathbf{H}, \mathbf{T}) = \mathbf{0}, \qquad \mathbf{R}_{\breve{\eta}}(\mathbf{H}; \mathbf{U}, \mathbf{T}) = \mathbf{0}, \qquad \mathbf{R}_T(\mathbf{T}; \mathbf{U}, \mathbf{H}) = \mathbf{0}. \tag{68}$$

A monolithic scheme is employed to solve the coupled nonlinear equations (68) so that they are solved simultaneously with respect to all unknowns using the Newton method with the corresponding residual form reading

$$\bar{\mathbf{R}}(\bar{\mathbf{U}}) = \mathbf{0}, \qquad \bar{\mathbf{R}} = \{\mathbf{R}_{\boldsymbol{\varphi}}, \mathbf{R}_{\breve{\eta}}, \mathbf{R}_T\}, \qquad \bar{\mathbf{U}} = \{\mathbf{U}, \mathbf{H}, \mathbf{T}\}. \tag{69}$$

The automatic differentiation (AD) technique implemented in the *AceGen* system (Korelc, 2009; Korelc and Wriggers, 2016) is used to obtain the exact algorithmic tangent required by the Newton method. The constitutive description is based on the logarithmic transformation strain, cf. Eq. (18), and hence the matrix exponential and its first and second derivatives are needed in the implementation of the model. The closed-form representation of the matrix exponential (Korelc and Stupkiewicz, 2014; Hudobivnik and Korelc, 2016), which is available in *AceGen*, is used for that purpose. The computations are carried out using *AceFEM*, a flexible finite-element environment that is interfaced with *AceGen*. A direct linear solver (Intel MKL PARDISO) has been used in all computations reported below.

4. Numerical examples

4.1. NiTi dog-bone specimen in tension

In this subsection, the effect of the loading rate on the macroscopic response and on the pattern of Lüders-like bands is studied for a NiTi dog-bone specimen in tension with reference to the experimental study of Zhang et al. (2010). The same experiment has been simulated in our earlier work using a 1D model (Rezaee-Hajidehi and Stupkiewicz, 2018), and the respective results are reported below for comparison.

The geometry and finite-element mesh are depicted in Fig. 2. The loading is applied by prescribing the overall elongation at the ends of the specimen with a constant loading velocity. At the same time, each end is constrained to behave as a rigid plane that is allowed to rotate with respect to the axis normal to the specimen plane so that the in-plane bending is prevented. This
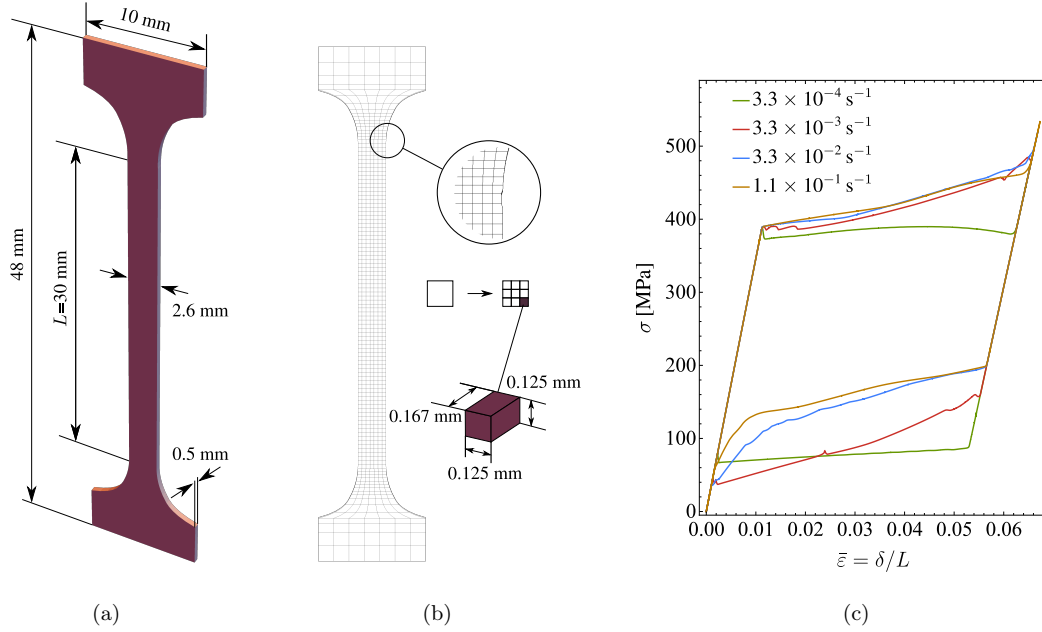
Figure 2: NiTi dog-bone specimen in tension: (a) the geometry, (b) the mesh and (c) the average stress–normalized elongation response corresponding to four representative loading rates. The mesh used in the computations was three times finer than that shown in figure (b), as schematically indicated in the inset.

approximates the loading applied in the experiment through pin-hinge connectors. After reaching the maximum overall elongation of $2.35\,\mathrm{mm}$, the specimen is unloaded. As in the experiment, the nominal loading rate, defined as the velocity at the grips normalized by the gauge length L, is varied between 1.1×10^{-4} and $1.1 \times 10^{-1}\,\mathrm{s}^{-1}$. The elongation δ, which is used later to characterize the average stress–normalized elongation response, is determined for the gauge segment of the length $L = 30\,\mathrm{mm}$.

Considering that the grips effectively act as heat sinks, the temperature is prescribed at both ends to the initial temperature $T_0 = 296\,\mathrm{K}$. In order to account for the heat exchange between the specimen and the surrounding, a value of the heat convection coefficient typical for stagnant air is adopted, $h = 6\,\mathrm{W/(m^2\,K)}$. Note that, depending on the ambient environment, the effect of heat convection varies considerably. For a stagnant air, the effect of heat convection is small, and the transient response is mostly controlled by the heat conduction (Iadicola and Shaw, 2004; He and Sun, 2010b).

The material parameters of the NiTi alloy, assumed here isotropic, are provided in Table 1. With the exception of the elastic moduli κ and μ and the transformation strain in compression ϵ_C, which are not apparent in the 1D model, the material parameters are here adopted equal to those used in the 1D simulations in our previous work (Rezaee-Hajidehi and Stupkiewicz, 2018), so that a direct comparison of 1D and 3D results is possible and meaningful. The shear modulus μ, assumed

20

Table 1: Material parameters used for the simulation of the NiTi dog-bone specimen.

κ [GPa]	μ [GPa]	H [MPa]	f_{c} [MPa]	T_{t} [K]	Δs^* [MPa/K]	ϱ_0 [kg/m^3]	c [J/(kg K)]	K [W/(m K)]	ϵ_{T} [-]	ϵ_{C} [-]	G [Pa m^2]	χ [MPa]
133	12	-2.2	6.8	224	0.24	6500	440	18	0.049	0.035	0.014	116

identical for austenite and martensite, corresponds to the Young's modulus $E = 35\,\mathrm{GPa}$, as in the previous work, and to the bulk modulus $\kappa = 133\,\mathrm{GPa}$, which is in the typical range for NiTi. The maximum transformation strains in tension and in compression are adopted as $\epsilon_{\mathrm{T}} = 0.049$ and $\epsilon_{\mathrm{C}} = 0.035$, respectively. The former is taken from the previous work, the latter corresponds to the typical ratio $\alpha = \epsilon_{\mathrm{T}}/\epsilon_{\mathrm{C}} = 1.4$. Note that the tension–compression asymmetry does not visibly influence the response, since the specimen is here loaded in tension only. For the same reason, the softening modulus H is here assumed independent of the deformation mode, i.e. $H_{\mathrm{T}} = H_{\mathrm{C}} = H$.

As discussed in detail by Rezaee-Hajidehi and Stupkiewicz (2018), parameter $G = 0.014\,\mathrm{Pa\,m}^2$, which controls the gradient effects, corresponds to the theoretical thickness of the interface equal to $0.25\,\mathrm{mm}$ (for $H = -2.2\,\mathrm{MPa}$), see Section 4.3. The micromorphic regularization parameter $\chi = 116\,\mathrm{MPa}$ ensures that the micromorphic variable $\breve{\eta}$ approximates the volume fraction η sufficiently well (the averaging length scale ℓ, Eq. (41), is equal to $0.011\,\mathrm{mm}$ which is small compared to the interface thickness of $0.25\,\mathrm{mm}$).

The gauge segment of the specimen is discretized with 21 elements across the width, 3 elements through the thickness, and 240 elements along the length, while the mesh gets coarser towards the grip segments which do not transform. Note that, for better visualization, the mesh shown in Fig. 2b is three times coarser than that actually used in the computations. The total number of elements is 20 664, and the total number of degrees of freedom is 650 999. The related computational cost strongly depends on the loading rate. In the case of the highest loading rate, the complete loading-unloading cycle is completed in 179 steps with the average of 6–7 iterations per step. Note that an adaptive time stepping procedure is used. In terms of the computation time, the complete simulation takes then less than 5 hours on a 10-core workstation (Intel Core i7-6950X CPU with 128 GB RAM). In the case of the lowest loading rate, 820 steps are needed to complete the simulation with the total computation time of nearly 21 hours.

To trigger the nucleation of the phase transformation, a small indentation, with the depth of 0.02 of the specimen thickness, is imposed at the top tapered end of the specimen, see Fig. 2b. It has been checked that without the imperfection, due to the symmetry of the specimen, the transformation initiates simultaneously at both ends of the gauge segment, which is not realistic. The nucleation stress is then slightly higher than in the case with imperfection. As shown below, despite the imperfection, nearly symmetric transformation patterns develop for higher loading rates.

The results obtained for four representative loading rates (out of the total of eleven cases simulated) are presented in detail in Figs. 3–6. For each loading rate, the corresponding figure shows the average stress–normalized elongation curve and the series of snapshots that illustrate the transformation pattern represented by the evolution of η and the evolution of temperature. Each average stress–normalized elongation curve is compared to the one predicted by the 1D model (Rezaee-Hajidehi and Stupkiewicz, 2018) and to the experimental one (Zhang et al., 2010). Here, the average stress is the nominal stress, i.e. the axial force divided by the initial cross-section area, and the elongation δ is normalized by the gauge length L so that $\bar{\varepsilon} = \delta/L$ represents the average axial strain within the gauge segment.

The complex rate-dependent response illustrated in Figs. 3–6 is the result of the interplay between the instabilities and strain localization caused by the intrinsic softening response of the material on one hand and the thermomechanical coupling and transient heat conduction effects on the other hand. Recall that the latent heat of transformation is released during the forward transformation and absorbed during the reverse transformation. The related increase of temperature during the forward transformation is then more pronounced for higher loading rates, with nearly adiabatic conditions at the highest loading rate, while the response is nearly isothermal for the lowest loading rate, as there is then enough time for the heat to flow to the grips which act as heat sinks. The local increase of temperature leads to the increase of the transformation stress, because the chemical energy of transformation $\Delta\phi_0$ increases with increasing temperature, cf. Eqs. (44) and (A.6). As a result, the hardening-type behaviour is observed for higher loading rates. This is illustrated in Fig. 2c which compares the average stress–normalized elongation curves predicted for the four selected loading rates.

The second major coupling effect is related to the strain localization which leads to the temperature inhomogeneity. The local increase of temperature caused by nucleation of a martensite band may hinder the transformation in that region due to the related increase of the transformation stress. The transformation may then proceed in another region where the temperature and thus also the transformation stress are lower. This leads to the development of complex transformation patterns, depending on the loading rate and transient heat conduction effects.

For the lowest loading rate of $3.3 \times 10^{-4}\,\mathrm{s}^{-1}$, Fig. 3, the transformation initiates at the imperfection at the stress of approximately 400 MPa, which is identical for all strain rates, see Fig. 2c. Initially, the martensite band is inclined with the inclination angle of approximately 57° with respect to the loading axis. Subsequently, the inclined interface transforms to a butterfly-shaped interface and the latter pattern remains for the rest of the loading stage. The interface pattern changes so as to avoid the lateral misalignment caused by the local kinking at the inclined interface and, consequently, to reduce the resulting bending moment. The butterfly-shaped pattern can be
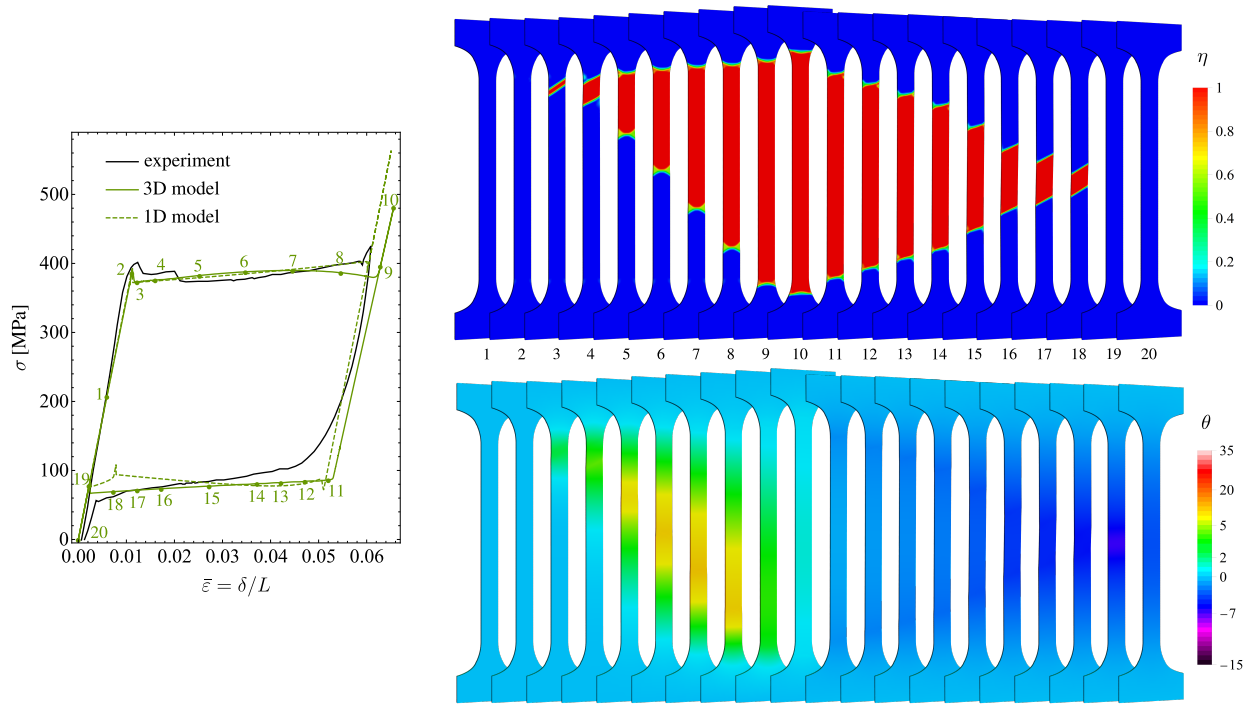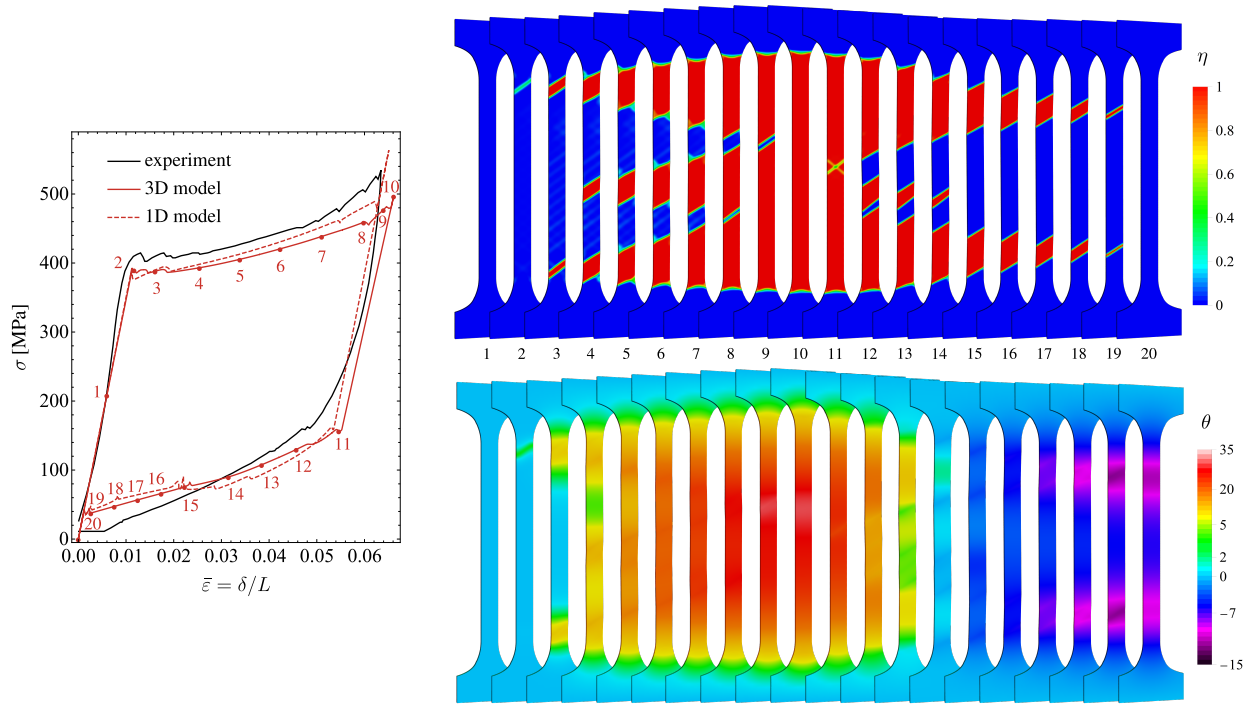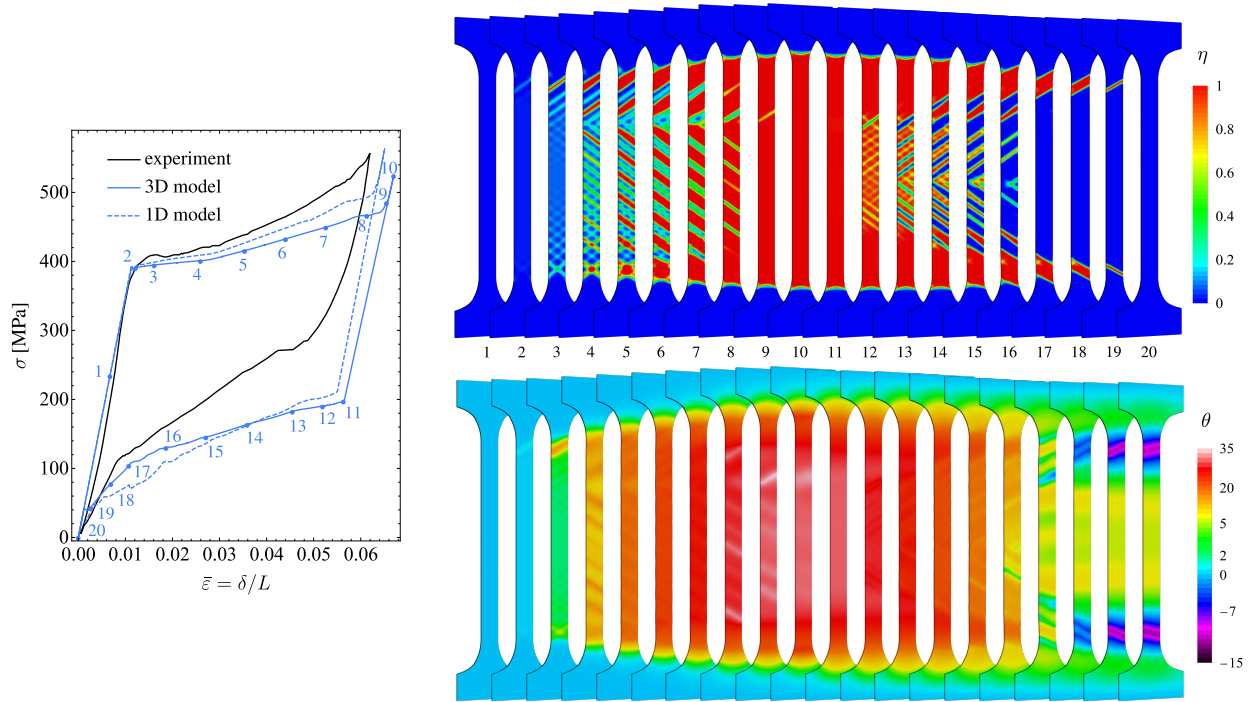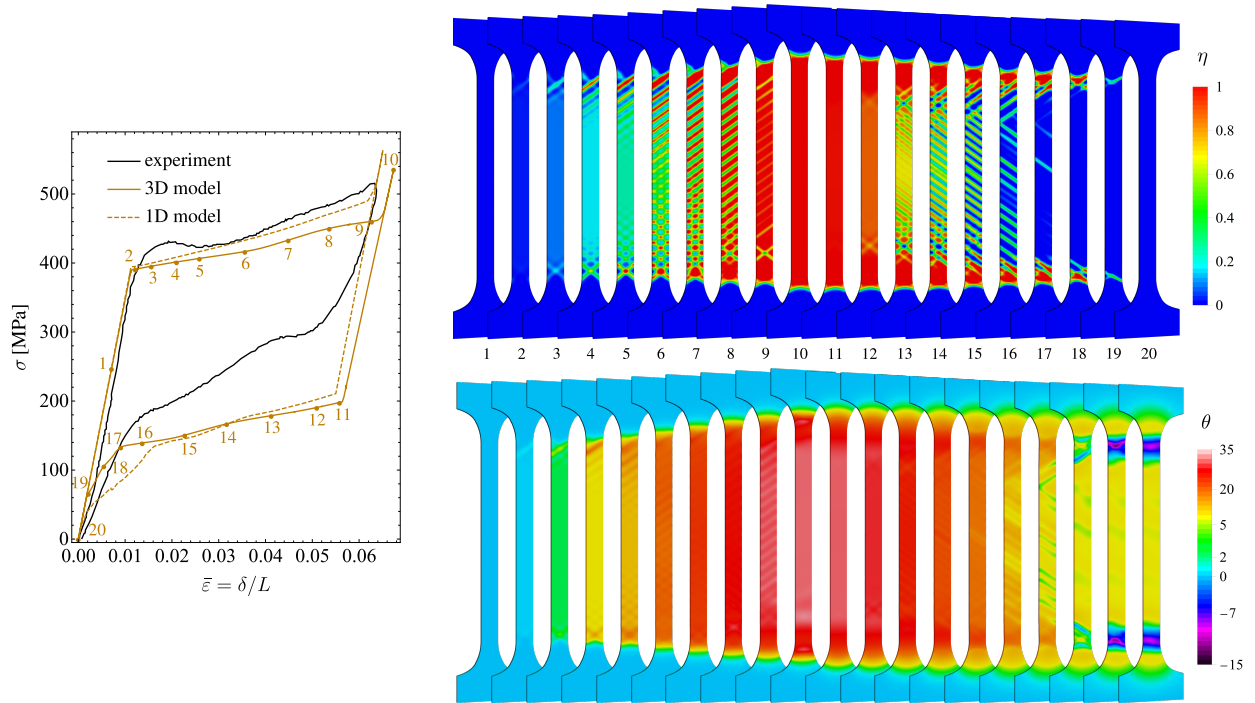
Figure 3: The average stress–normalized elongation curves (left), the transformation pattern (upper-right) and the evolution of the relative temperature $\theta = T - T_0$ (lower-right) for the loading rate $3.3 \times 10^{-4}\,\mathrm{s}^{-1}$.

Figure 4: The average stress–normalized elongation curves (left), the transformation pattern (upper-right) and the evolution of the relative temperature $\theta = T - T_0$ (lower-right) for the loading rate $3.3 \times 10^{-3}\,\mathrm{s}^{-1}$.

Figure 5: The average stress–normalized elongation curves (left), the transformation pattern (upper-right) and the evolution of the relative temperature $\theta = T - T_0$ (lower-right) for the loading rate $3.3 \times 10^{-2}\,\mathrm{s}^{-1}$.

Figure 6: The average stress–normalized elongation curves (left), the transformation pattern (upper-right) and the evolution of the relative temperature $\theta = T - T_0$ (lower-right) for the loading rate $1.1 \times 10^{-1}\,\mathrm{s}^{-1}$.

interpreted as a representation of the so-called criss-cross pattern that is often seen in the experiment, see e.g. Shaw and Kyriakides (1997), Zhang et al. (2010), Kim and Daly (2011), which, however, does not form because the finite-element mesh is too coarse (Shaw, 2000). Our auxiliary simulations confirm that, upon mesh refinement, the butterfly-shaped pattern is substituted by the criss-cross pattern. During unloading, the reverse transformation proceeds by a backward motion of the two butterfly-shaped interfaces which convert into inclined interfaces at the end of the process.

For the loading rate of $3.3 \times 10^{-3}\,\mathrm{s}^{-1}$, Fig. 4, again the transformation starts at the imperfection. However, shortly after that, the second martensite domain forms at the other end of the specimen as a result of the temperature increase in the first domain, and then the third domain nucleates in the middle. Subsequently, the three domains expand, while maintaining the inclined pattern, and finally coalesce at the end of the loading stage. During unloading, the reverse transformation starts by nucleation of the bands of austenite in the middle where the temperature is the highest. Then, the austenite domains grow at the expense of the martensite domains until the latter disappear. As the loading rate is further increased, the number of martensite domains increases. Apart from that, for high loading rates, the responses are qualitatively similar to each other, and the interfaces are predominantly inclined, sometimes accompanied by secondary features.

The average stress–normalized elongation curves, both numerical and experimental, display kinks that accompany the nucleation and annihilation events. Specifically, during the forward transformation, nucleation of martensite bands and annihilation of austenite bands is associated with a stress drop. Likewise, during the backward transformation, nucleation of austenite bands and annihilation of martensite bands is associated with a stress rise. The respective effects have been illustrated and discussed in detail by Zhang et al. (2010).

Figure 7 shows the maximum number of martensite domains during loading as a function of the loading rate. The dependence is approximately linear on the log-log plot, which indicates a power-law-type relationship. Power-law fitting gives the exponent of 0.49 which is very close to the exponent of 0.5 obtained by fitting the experimental data (cf., Zhang et al., 2010) and also resulting from the theoretical considerations (cf., He and Sun, 2010b). For comparison, the results of the 1D model (Rezaee-Hajidehi and Stupkiewicz, 2018) are also included in Fig. 7.

The average stress–normalized elongation curves show a reasonably good agreement with the experimental curves, see Figs. 3–6. The differences are more pronounced at higher loading rates, particularly during the reverse transformation. Note, however, that the constitutive model, with its intrinsic trilinear response, see Fig. 1a, is too simple to describe the complex constitutive behaviour of pseudoelastic NiTi. Also, it is recalled that the material parameters are here taken directly from the 1D model (Rezaee-Hajidehi and Stupkiewicz, 2018) without any tuning or fitting. The average stress–normalized elongation curves predicted by the 3D and 1D models show small differences, see
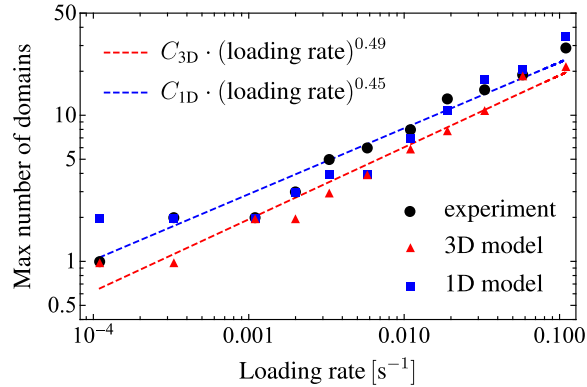
Figure 7: The maximum number of martensite domains during loading as a function of the loading rate: predictions of the 3D and 1D models are compared to the experimental data of Zhang et al. (2010). The dashed lines depict the power-law fit of the respective model predictions, which are characterized by the exponent close to 0.5.
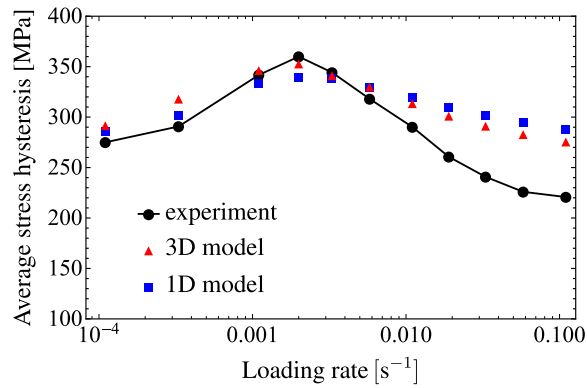

Figure 8: The average stress hysteresis as a function of the loading rate.

Figs. 3–6, which are mostly due to the finite-deformation effects included in the present 3D model. In fact, the results obtained for the small-strain version of the 3D model, which are not reported here, are very close to the results of the 1D model.

The dependence of the average stress hysteresis on the loading rate is shown in Fig. 8. The average stress hysteresis is here defined as the area of the hysteresis loop on the average stress–normalized elongation curve divided by $\epsilon_{\rm T}$, the maximum transformation strain in tension. In agreement with the experiment, the dependence is non-monotonic with the maximum at the loading rate of $2 \times 10^{-1}\,{\rm s}^{-1}$. For high loading rates, the stress hysteresis predicted by the model is visibly higher than in the experiment. The predictions of the 1D model (Rezaee-Hajidehi and Stupkiewicz, 2018), also shown in Fig. 8, are similar to those of the 3D model.

In order to examine the effect of mesh density on the results, additional computations have been performed for selected loading rates using a coarser and a finer mesh. In the case of the coarse mesh,

the gauge segment is discretized into $120{\times}10{\times}2$ elements, i.e. the element size is approximately twice larger than in the case of the reference mesh of $240{\times}21{\times}3$ elements, so that the total number of degrees of freedom is $122\,657$. In the case of the fine mesh, the gauge segment is discretized into $480{\times}42{\times}4$ elements so that the in-plane mesh density is twice that of the reference mesh, while the through-the-thickness density is only slightly increased to avoid an excessive increase of the total number of degrees of freedom, which is now equal to $3\,294\,517$. Note, however, that the unknown fields do not exhibit significant changes in the normal direction, hence the in-plane mesh density is more important for an accurate resolution of the transformation patterns formed.

Figure 9 shows the results obtained for the loading rate of $3.3 \times 10^{-3}\,\mathrm{s}^{-1}$. The average stress–normalized elongation curves obtained for the three mesh densities show only minor differences. In the enlarged views in Fig. 9, the differences are visible during nucleation of the three bands of martensite during forward transformation (each nucleation event is associated with a stress drop) and during nucleation of the two bands of austenite during reverse transformation (each nucleation event is associated with a stress rise). Likewise, small differences are visible at the instants of annihilation of the austenite and martensite bands, as indicated by the arrows in Fig. 9. The transformation pattern is not significantly affected by the mesh density either. Figure 9 shows representative transformation patterns corresponding to the instants marked by 4 and 12 in Fig. 4. In the case of the fine mesh, the appearance seems different, however, rotation by 180°, as indicated in Fig. 9, reveals that the transformation pattern is indeed essentially identical.

In the case of the loading rate of $3.3 \times 10^{-2}\,\mathrm{s}^{-1}$, the effect of mesh density on the average stress–normalized elongation curve is also negligible, see Fig. 10. Small differences are only observed during annihilation events, i.e. at the end of the forward and reverse transformations. Similarly, the transformation pattern is slightly influenced by the mesh density. The pattern corresponding to the instant marked by 3 is identical for the three mesh densities. Though some differences can be observed at the later stages, the important features, such as the number of martensite bands, are preserved. During the reverse transformation, the effects are qualitatively similar, and the corresponding details are not provided here for brevity.

4.2. NiTi tube in tension

In this subsection, the simulation is carried out for the problem of uniaxial tension of a pseudo-elastic NiTi tube. The problem has been studied experimentally by Bechle and Kyriakides (2016), and its extensive computational study has been performed by Jiang et al. (2017b). Earlier experimental investigations of uniaxial and combined tension of NiTi tubes include those of Sun and Li (2002), Feng and Sun (2006), Reedlunn et al. (2014), and others.

Figure 11 depicts the geometry and the finite-element mesh used in the simulation. Following Jiang et al. (2017b), idealized boundary conditions are applied in the simulation, since the actual
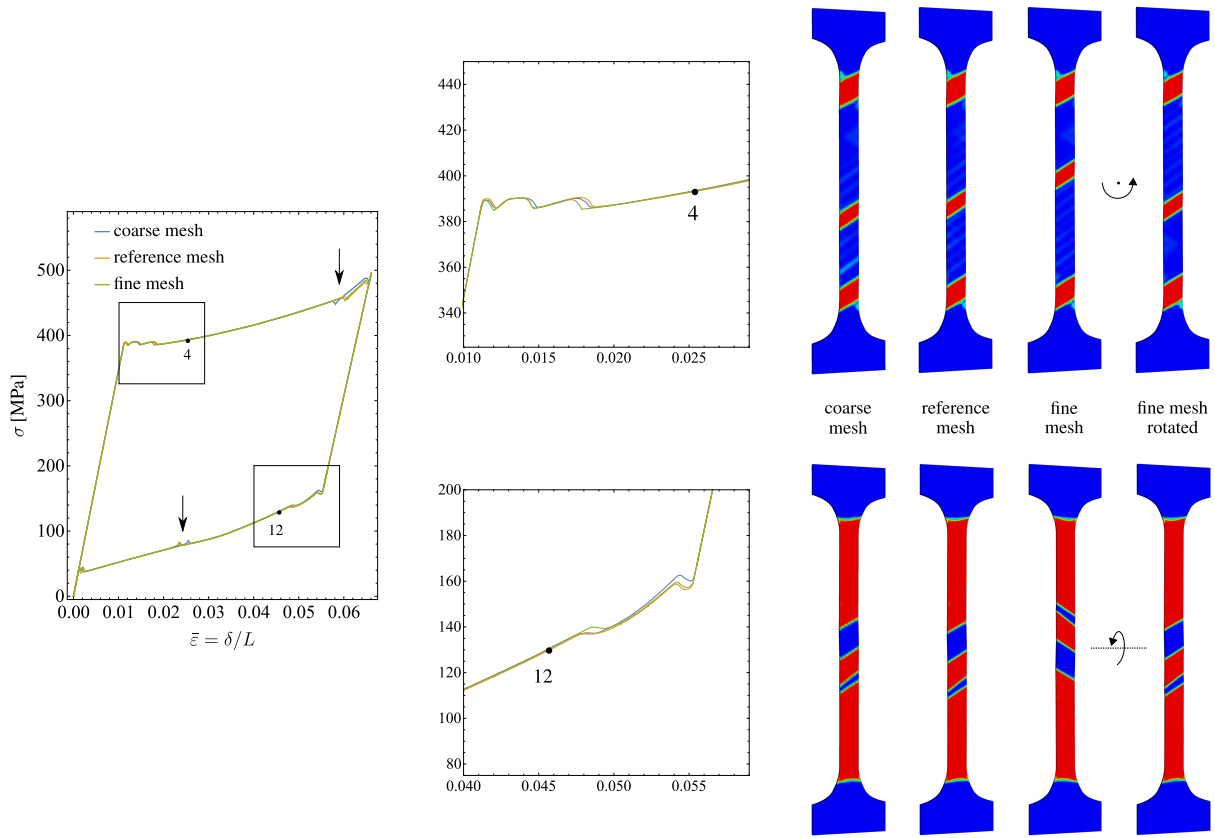
Figure 9: The effect of mesh density for the loading rate of $3.3 \times 10^{-3}\,\mathrm{s}^{-1}$. The average stress–normalized elongation curves obtained for three mesh densities are shown (left) along with the enlarged view of the events of nucleation of martensite bands during loading (center, top) and austenite bands during unloading (center, bottom). The transformation patterns at the instants marked by 4 and 12 are also shown (right), cf. Fig. 4.
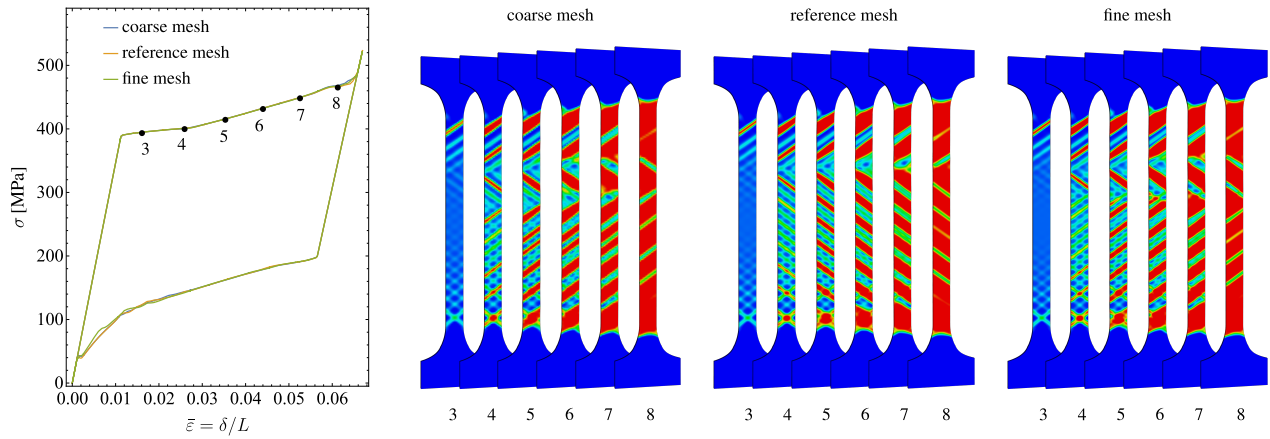

Figure 10: The effect of mesh density for the loading rate of $3.3 \times 10^{-2}\,\mathrm{s}^{-1}$: the average stress–normalized elongation curve (left) and the transformation pattern during the forward transformation (right).

28
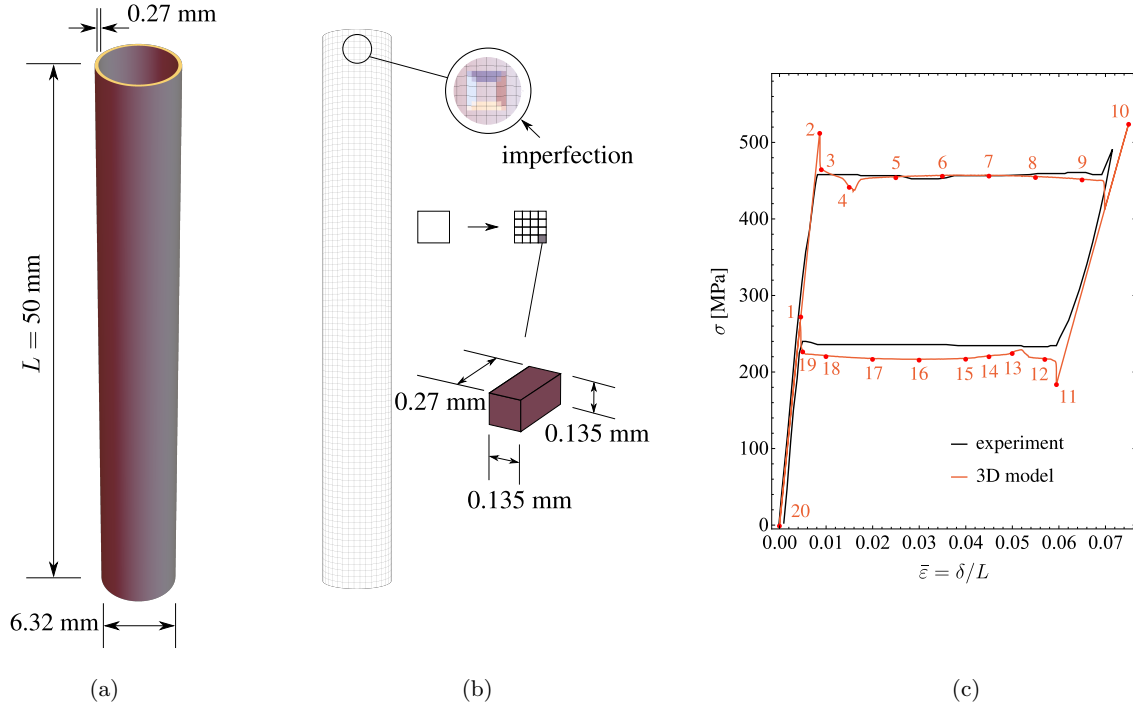
Figure 11: NiTi tube in tension: (a) the geometry, (b) the mesh and (c) the average stress–normalized elongation response. The mesh used in the computation was four times finer than that in figure (b), as schematically indicated in the inset. The average stress σ is calculated as the axial force divided by the initial cross-section area of the tube.

boundary conditions used in the experiment are too complex to be fully reproduced. Specifically, the axial displacement is prescribed on the top of the tube with a constant loading rate of $5 \times 10^{-5}\,\mathrm{s}^{-1}$, as in the experiment. After reaching the maximum elongation of $3.7\,\mathrm{mm}$, the specimen is unloaded. Concerning the lateral displacements at both ends, rotation of the tube with respect to its axis is constrained, and a uniform expansion or contraction is allowed by applying the following boundary condition: $x_i Y_i - y_i X_i = 0$, where (X_i, Y_i) and (x_i, y_i) are, respectively, the reference and current placement of the i-th node within the plane normal to the axis. To approximate the effect of the grips, the temperature of both ends is fixed to the ambient temperature $T_0 = 296\,\mathrm{K}$. In view of the low loading rate, which results in nearly isothermal conditions, the heat convection effect is neglected.

The material is considered isotropic and the material parameters are adopted as follows. The bulk modulus $\kappa = 133$ GPa is adopted. The different shear moduli for pure austenite and pure martensite phases, i.e., $\mu_\mathrm{a} = 21$ GPa and $\mu_\mathrm{m} = 8$ GPa, are fitted, respectively, to the corresponding branches in the experimental response, see the black curve in Fig. 11c. The material parameters $\Delta s^* = 0.24\,\mathrm{MPa/K}$, $T_\mathrm{t} = 211\,\mathrm{K}$, $f_\mathrm{c} = 6.8\,\mathrm{MPa}$, $\epsilon_\mathrm{T} = 0.05$, and $H_\mathrm{T} = -2.8\,\mathrm{MPa}$ are calibrated such that the average stress–normalized elongation curve in the simulation correctly reproduces the experimental one, cf. Fig. 11c. In particular, the softening modulus H_T is adopted so as to approx-

29

imately match the softening tensile stress-strain curve determined by Hallai and Kyriakides (2013) and used by Jiang et al. (2017b). The hardening modulus in compression $H_C = 10\,\text{MPa}$, which does not visibly affect the overall response in tension, is adopted based on the typical homogeneous response of NiTi under compression (Reedlunn et al., 2014; Bechle and Kyriakides, 2014). Note that the difference in the elastic moduli of austenite and martensite introduces additional softening in the intrinsic stress–strain response. The parameters $\alpha = 1.4$, $\varrho = 6500\,\text{kg/m}^3$, $c = 440\,\text{J/(kg\,K)}$ and $K = 18\,\text{W/(m\,K)}$ are taken as those in the dog-bone simulation, Section 4.1. Finally, the parameter $G = 0.01\,\text{Pa\,m}^2$ is adopted such that the theoretical thickness of the interface is equal to $0.2\,\text{mm}$, while the parameter $\chi = 293\,\text{MPa}$ is sufficiently large to ensure that the micromorphic variable $\breve{\eta}$ approximates well the volume fraction η (the corresponding averaging length $\ell = 0.006\,\text{mm}$ is small compared to the interface thickness).

The tube is discretized with 147 elements in the circumferential direction, one element through the thickness and 370 elements along the height, giving the total number of $54\,684$ elements and $2\,178\,246$ degrees of freedom (recall that quadratic elements are used). For better visualization, the mesh shown in Fig. 11b is four times coarser than the actual mesh used in the simulation. The associated computational cost is quite high. A single Newton iteration takes about 49 seconds of which the solution of the linear system takes about 42 seconds (recall that a direct solver is used). Furthermore, a relatively small time step is needed to resolve the fine features of the transformation pattern evolution, so that the total number of time steps exceeds 3700. As a result, the complete simulation takes about 18 days on a 10-core workstation (Intel Core i7-6950X CPU with 128 GB RAM).

To trigger the nucleation of the phase transformation, a small imperfection, in the form of a uniform indentation with the depth of 0.02 of the tube thickness, is imposed at the top of the tube, see Fig. 11b.

The markers that are superimposed on the average stress–normalized elongation response in Fig. 11c correspond to the snapshots presented in Fig. 12, which show the transformation pattern in the deformed configuration. To track the transformation pattern completely, the front view with 0° rotation, the side view with 90° rotation and the back view with 180° rotation are presented.

The martensite bands nucleate at the imperfection forming two helix-shaped bands winding around the tube in opposite directions and colliding at the back of the tube. Albeit the imperfection is symmetric, the transformation does not nucleate symmetrically, see the back-view snapshots 2 and 3 in Fig. 12. The nucleation event is associated with a stress overshoot followed by a sudden stress drop. The related effects, not visible in the experimental curve, but often encountered in other experiments, see e.g. Li and Sun (2002), are highly sensitive to the experimental setup, specimen geometry, type and strength of the imperfection (Churchill et al., 2009).
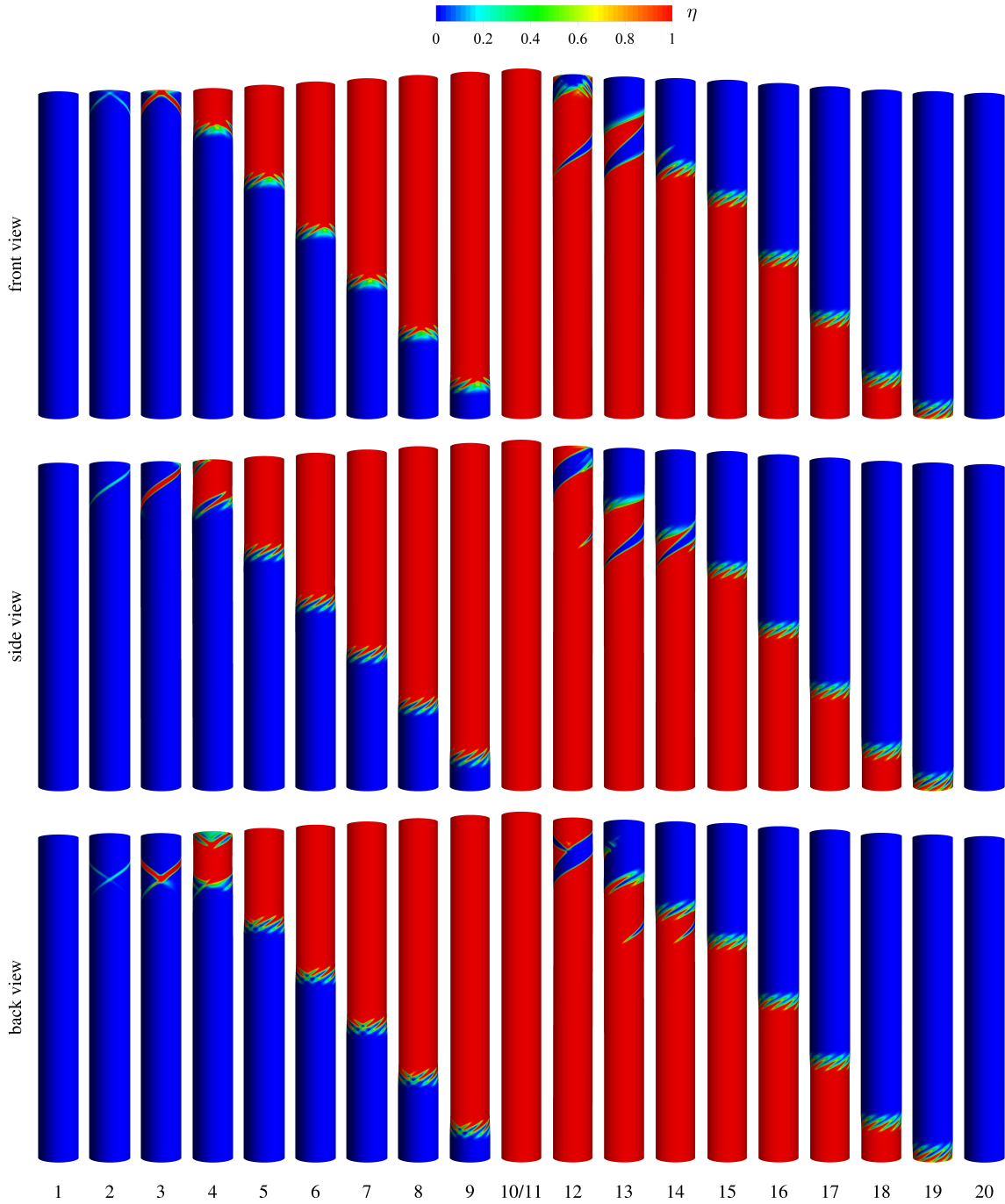
Figure 12: The transformation pattern of the NiTi tube: the front view (top), the side view (middle) and the back view (bottom). Since the transformation patterns of snapshots 10 and 11 are identical, only snapshot 10 is presented.
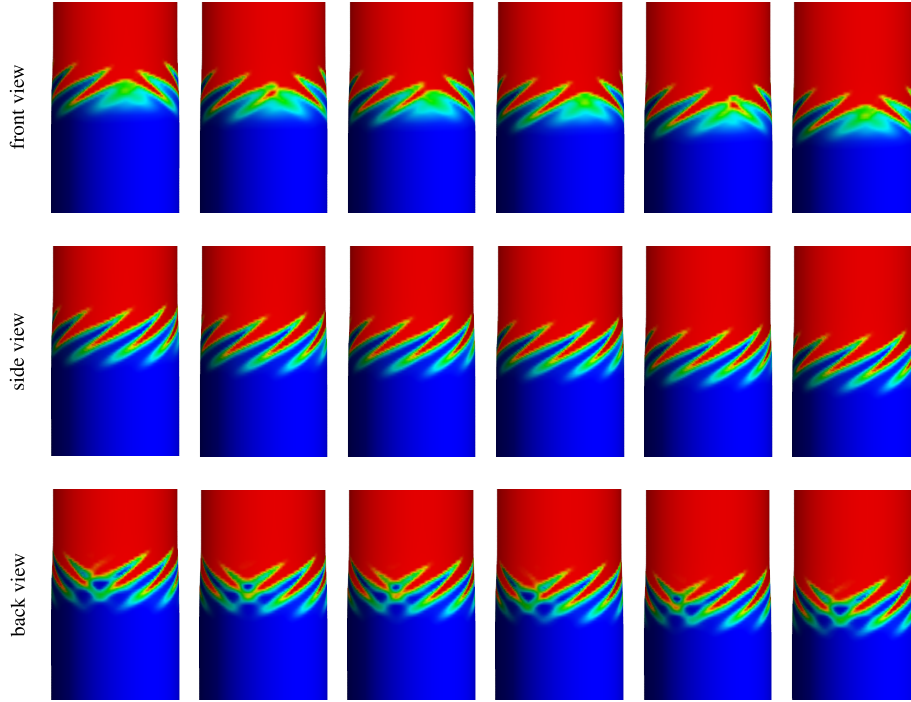
Figure 13: Detailed view of the formation and coalescence of martensite prongs during loading: the front view (top), the side view (middle) and the back view (bottom).

After the nucleation, in the neighbourhood of point 4, a stress drop is observed on the average stress–normalized elongation curve. In Fig. 12, this corresponds to the complete transformation of the top part of the tube. Henceforth, the transformation propagates in a prong-like pattern in which the prongs form at the front of the tube, then propagate around the tube helically and eventually coalesce into the martensite domain at the back of the tube. This periodic event is shown in the expanded view of the transformation pattern in Fig. 13. The two successive prongs circle the tube in opposite directions with an inclined angle of approximately $\pm 57°$ with respect to the tube axis, in agreement with the experimental observations (Li and Sun, 2002; Feng and Sun, 2006; Reedlunn et al., 2014). From Fig. 13 it can be readily seen that the transformation does not propagate symmetrically and changes its orientation as a new prong forms or coalesces. The martensite domain propagates with the same periodic pattern until the complete transformation of the tube. The pattern of the quasi-symmetric multi-prong interface illustrated in Fig. 13 is essentially identical to that predicted by Jiang et al. (2017b). It is evident from Fig. 11c that, due to the nearly isothermal conditions, the average stress is almost constant in the plateau region, except for the stress drops in the neighbourhood of point 4 and at the end of the forward transformation.

During unloading, similar to the loading stage, a stress rise in the neighbourhood of point 13 is observed, which is associated with the complete reverse transformation of the top part of the
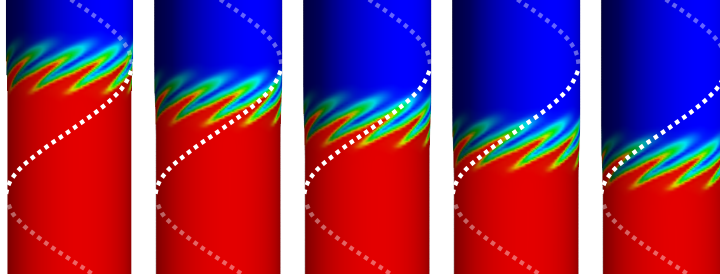
Figure 14: Detailed view of the steady-state propagation of the multi-prong transformation front during unloading. Each prong propagates along a helical path, as indicated by the white dashed line.

tube. Hereafter, the stress is almost constant, and the reverse transformation proceeds in the form of helical prongs that propagate in a different manner than those during loading. Fig. 14 shows the expanded view of the reverse transformation during the steady-state propagation. In this case, all helical prongs propagate simultaneously, in the same direction following helical paths inclined at the angle of approximately 57° with respect to the tube axis, and eventually annihilate at the bottom of the tube. The helical trajectory of the prongs is more apparent when the helix of one of the propagating prongs is superimposed on the transformation pattern, see the white dashed curve in Fig. 14. The annihilation of the martensite domains at the bottom of the tube, which completes the reverse transformation, is associated with a sudden stress rise.

As also discussed by Bechle and Kyriakides (2016), the very low loading rate leads to a nearly uniform temperature distribution in the tube during both loading and unloading. The maximum temperature increase during loading is obtained as $\theta = 2.2\,\mathrm{K}$, while for unloading, the minimum temperature decrease of $\theta = -2.0\,\mathrm{K}$ is recorded.

The transformation pattern obtained, Figs. 12–14, is qualitatively similar to that observed in the experiment (Bechle and Kyriakides, 2016), see also Feng and Sun (2006) and Reedlunn et al. (2014). This, in particular, concerns formation of the multi-prong transformation front and helical propagation path of individual prongs. However, as illustrated by the computational study of Jiang et al. (2017b), the details of the complex transformation pattern are influenced by the model parameters, e.g., the softening modulus, and are sensitive to the imperfection, e.g., to its position and symmetry.

The latter effect is illustrated in Fig. 15. The quasi-symmetric pattern shown in Fig. 12 has been obtained for a symmetric imperfection, cf. Fig. 11b. The transformation pattern is different when an asymmetric imperfection is introduced. Specifically, it initiates with a single helical band, and the transformation proceeds then by elongation and thickening of this single band. At a later stage (not shown here), the helical band converts into a single martensite domain with a multi-prong
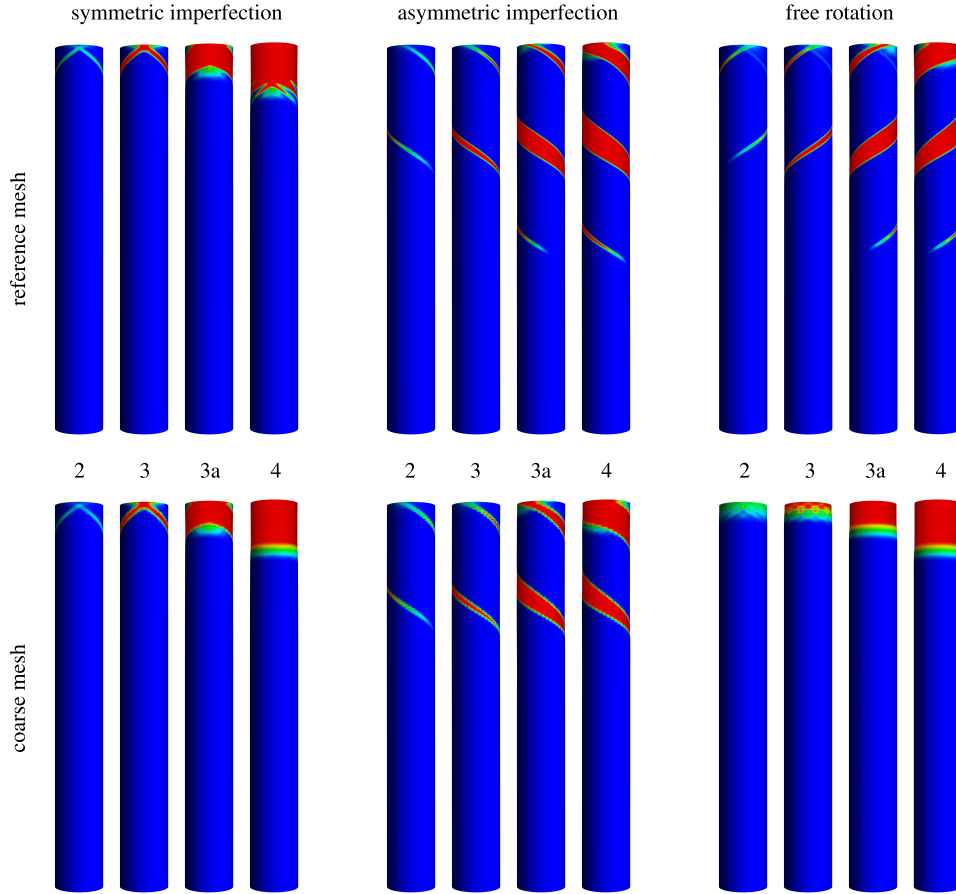
Figure 15: The effect of imperfection, boundary conditions and mesh density (see text) on the transformation patterns at the initial stage of transformation. Each snapshot number specifies the elongation, as indicated by the respective marker in Fig. 11c, see also Fig. 12. Snapshots 3a correspond to an intermediate elongation, $\bar{\varepsilon} = 0.012$.

interface of the type shown in Fig. 14. A single helical pattern develops also when the imperfection is symmetric but the boundary conditions are changed such that free rotation is allowed at the bottom, see Fig. 15. The orientation of the helical band is here different and results from a random numerical imperfection, since the problem is otherwise symmetric (in the case of the asymmetric imperfection, the orientation of the helical band is induced by the orientation of the imperfection). Note that the transformation pattern with a single helical band, as predicted here by changing the imperfection or the boundary conditions, has been observed experimentally in NiTi tubes under tension by Li and Sun (2002).

Figure 15 illustrates also the effect of mesh density on the transformation pattern. The three cases discussed above have been simulated using a coarser mesh of $74 \times 185 \times 1$ elements and $550\,708$ degrees of freedom, i.e. twice coarser in the circumferential and axial directions than the reference mesh of $147 \times 370 \times 1$ elements. In the original case, indicated as 'symmetric imperfection' in Fig. 15,

the initial pattern (snapshots 2 and 3) is correctly represented by the coarse mesh. However, at the later stage, the coarse mesh is not capable of representing the fine features of the multi-prong interface. In the case of asymmetric imperfection, a helical band forms, but it increases more in thickness than in length, as compared to the case of the reference mesh, and ultimately converts into a single domain (not shown here), as in the other coarse-mesh cases. On the contrary, in the case of free rotation, the helical band characteristic for the reference mesh does not form, and the pattern is symmetric, similar to the case of constrained rotation. In summary, the coarse mesh is too coarse to correctly represent the fine details of the transformation pattern that are obtained using the reference mesh. Computations have not been attempted for an even finer mesh because of a prohibitively high computational cost.

4.3. Parametric study of the features of the inclined macroscopic transformation front

In our previous study (Rezaee-Hajidehi and Stupkiewicz, 2018), it has been demonstrated that, in the 1D small-strain setting, the theoretical thickness λ of the diffuse interface (macroscopic phase transformation front) is a function of the softening modulus $H < 0$ and the gradient parameter $G > 0$ through the relation $\lambda = \pi\sqrt{-G/H}$. It has also been shown that, upon the micromorphic regularization, the thickness $\breve{\lambda}$, where $\breve{\lambda} \leq \lambda$, of the corresponding interface additionally depends on the regularization parameter χ, see Eq. (55) in Rezaee-Hajidehi and Stupkiewicz (2018), and $\breve{\lambda}$ approaches λ as χ increases. In the examples studied in the present paper, the parameter χ has been set in such way that $\breve{\lambda}/\lambda \geq 0.9$ so that the micromorphic regularization does not visibly influence the interface profile, see Figs. 5 and 6b in Rezaee-Hajidehi and Stupkiewicz (2018).

In the 3D setting, apart from the regularization resulting from the gradient term in the free energy, additional regularization is introduced due to the 3D geometry of the problem, in particular, due to the thickness of the specimen under study, see Mazière and Forest (2015). Accordingly, the aim of this numerical example is to examine the impact of the 3D effects on the characteristics of the macroscopic transformation front, namely the interface thickness and the inclination angle. Additionally, the influence of tension–compression asymmetry and transverse isotropy on the interface characteristics is studied.

The analysis is here carried out for a NiTi strip in uniaxial tension. Figure 16 depicts the geometry and the finite-element mesh. The strip is loaded by prescribing the overall elongation at its top end, while the transversal displacements of both ends are fully constrained. The strip is loaded up to the maximum elongation of 0.625 mm, which results in a partial transformation of the strip. To suppress the formation of more martensite bands, which might occur at higher loading rates, the strip is pulled with a constant low loading rate of $10^{-5}\,\mathrm{s}^{-1}$. Like in the previous examples, the temperature at both ends is set to the initial temperature $T_0 = 296\,\mathrm{K}$.
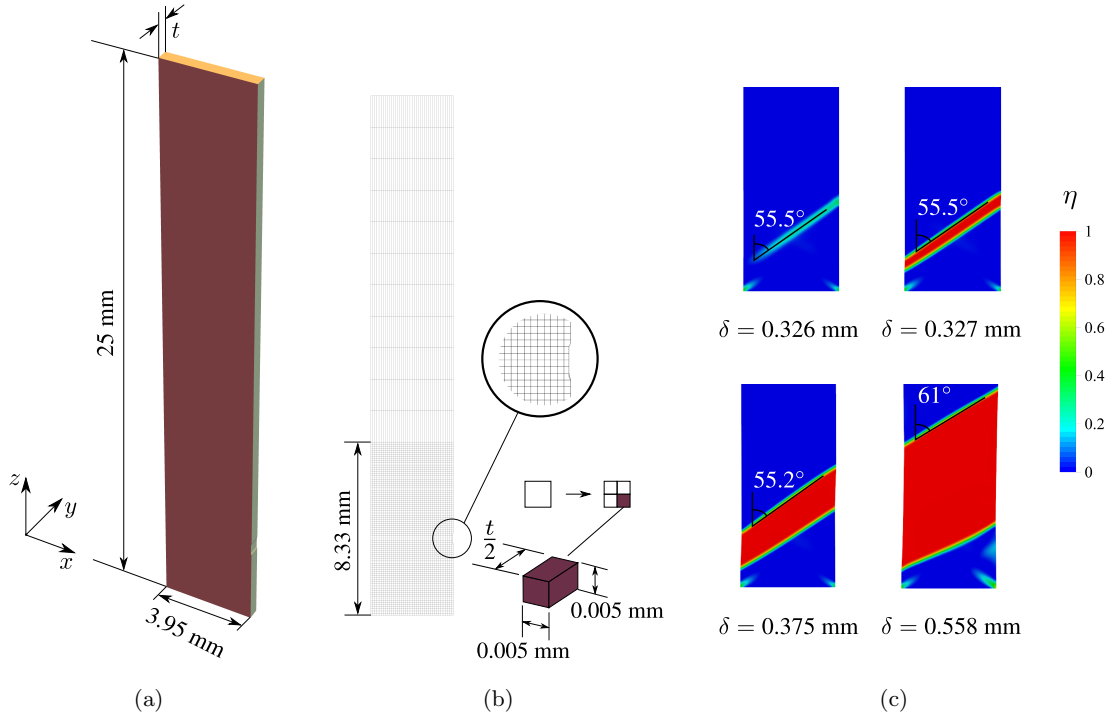
Figure 16: NiTi strip in tension: (a) the geometry, (b) the mesh and (c) the expanded view of the martensite band obtained for the strip with the thickness $t = 0.1\,\text{mm}$ at selected elongations δ.

To study the 3D effects, strips with different thicknesses, ranging from $t = 0.02$ mm to $t = 0.5\,\text{mm}$, are considered. The material parameters are adopted as those in the dog-bone example, Section 4.1, except that the softening modulus $H = -5\,\text{MPa}$ is chosen, the gradient parameter $G = 0.046\,\text{Pa}\,\text{m}^2$ is set to give the theoretical interface thickness $\lambda = 0.3\,\text{mm}$, and the regularization parameter $\chi = 262\,\text{MPa}$ is adopted such that sufficient regularization is applied (we have $\check{\lambda}/\lambda = 0.9$ and $\ell = 0.013\,\text{mm}$).

The mesh is finer in the lower part, where the band nucleates, and coarser in the upper part. The lower part of the strip is discretized with 79 elements across the width, 2 elements through the thickness, and 167 elements along the length. Note that, for a better visualization, the mesh shown in Fig. 16b is two times coarser than the one used in the simulation. The total number of elements is 29 862 with 990 345 degrees of freedom. To trigger the nucleation of the martensite band, a small imperfection, an indent with the depth of 0.02 of the strip thickness, is imposed at a distance equal to the width of the strip far from the bottom end, see Fig. 16b.

The interface thickness and the inclination angle are determined for the upper interface, which is not influenced by the boundary conditions at the bottom of the strip, see Fig. 16c. To this end, three equally spaced longitudinal profiles of the volume fraction η are taken at a fixed elongation $\delta = 0.375\,\text{mm}$. For each profile, the position of the interface and its thickness in the longitudinal

36

direction are determined by fitting a sine function to the profile. The positions are used to calculate the inclination angle, which is then used to determine the average interface thickness in the direction normal to the interface.

Figure 16c shows an expanded view of the martensite band obtained for the strip thickness $t = 0.1 \, \text{mm}$ (and for $\alpha = \beta = 1.4$). At the onset of transformation, the martensite band forms an angle of $55.5°$ with the strip axis, which is close to the theoretical angle of $54.74°$ for the necking-type discontinuity in thin sheets (Nadai, 1950; Hill, 1952), which has also been observed experimentally in NiTi strips under tension (e.g., Shaw and Kyriakides, 1997; He and Sun, 2010a) and predicted numerically (e.g., Shaw, 2000; He and Sun, 2010a; Jiang et al., 2017c; Wendler et al., 2017). The upper snapshots in Fig. 16c illustrate the actual nucleation event. A band of partially transformed material appears at the imperfection and grows towards the other side of the strip at fixed orientation. Once the band spans the whole strip width, the transformation strain within the band starts to increase, and, once the transformation is complete, the interfaces (mostly the top one) start to propagate. The inclination angle remains fairly constant as the elongation reaches $\delta = 0.375$ mm. At the further stage, the interface gradually changes its orientation and reaches $61°$ at $\delta = 0.558$ mm. The results obtained for the other thicknesses show that the effect of the strip thickness on the inclination angle is negligible.

The effect of the strip thickness on the interface thickness is shown in Fig. 17. As it is evident, the thicker the strip, the more regularization is provided, and consequently, the thicker the interface. On the other hand, as the strip thickness approaches zero, the accompanying regularization effect diminishes, and the interface thickness approaches the theoretical limit $\check{\lambda}$, see the dashed line in Fig. 17.

Next, the effect of tension–compression asymmetry and transverse isotropy is investigated. These properties are introduced in the model through the material parameters α and β in the function g that specifies the set of limit transformation strains, see Eqs. (23) and (25). Figure 18 shows the effect of parameters α and β on the inclination angle. Four cases are considered. In the case of an isotropic material, we have $\beta = \alpha$, and parameter α, which specifies the tension–compression asymmetry, is varied between 0.7 and 1.4, even if the range of $\alpha > 1$ is physically more relevant. In the case of transverse isotropy, $\beta \neq \alpha$, three cases are investigated, namely the symmetry axis $\boldsymbol{m}$ oriented along the x-, y- and z-directions, see Fig. 16a, parameter α is set to 1.4, and parameter β is varied between 0.7 and 1.4. The three cases are denoted as x-, y- and z-transversely isotropic, respectively. Note that the range of admissible values of parameters α and β is constrained by the required convexity of function g, cf. Section 2.1.1, and the adopted range between 0.7 and 1.4 is close to those limits.

For $\alpha \geq 1$ and $\beta \geq 1$, the inclination angle is weakly influenced by parameters α and β. In this
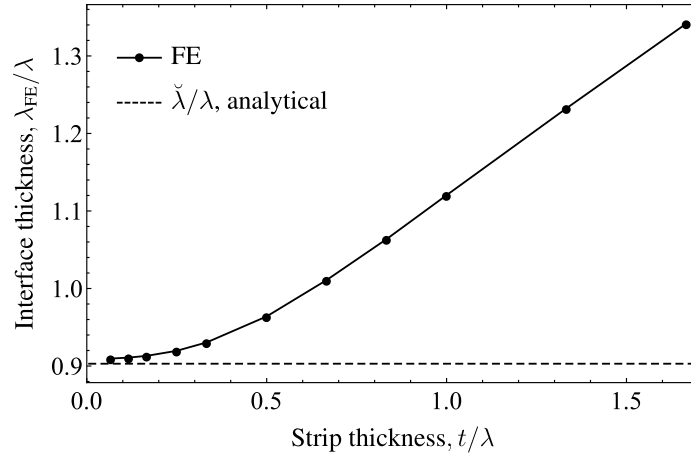
Figure 17: The dependence of the interface thickness on the thickness of the strip, both normalized by the theoretical thickness λ. The interface thickness is determined at the elongation $\delta = 0.375\,\text{mm}$. The dashed line represents the thickness $\breve{\lambda}$ that follows from the analytical solution obtained for the micromorphic 1D model, see Rezaee-Hajidehi and Stupkiewicz (2018).
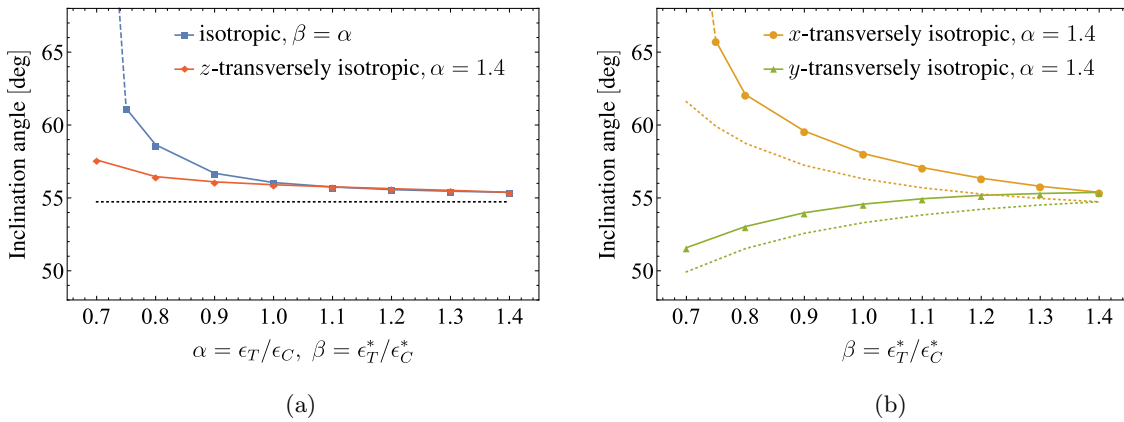

(a)

(b)

Figure 18: The effect of tension–compression asymmetry and transverse isotropy on the inclination angle. The dotted lines depict the theoretical predictions (see text).

range, the maximum deviation with respect to the reference case $\alpha = \beta = 1.4$ is below $3°$. Overall, for the y- and z-transversely isotropic cases, the inclination angle does not vary significantly and the maximum change of the inclination angle is, respectively, about $-4°$ and $2°$ at $\beta = 0.7$. On the other hand, for the isotropic and x-transversely isotropic cases, the inclination angle deviates considerably, and the interface tends to be perpendicular to the loading axis in the limit of $\alpha = \beta = 0.7$ and $\beta = 0.7$, respectively.

The dotted lines in Fig. 18 indicate the theoretical predictions of the inclination angle. Following the classical approach (Nadai, 1950; Hill, 1952), the interface between the transformed and untransformed zones is considered, and the inclination angle is found such that the inelastic elongation along the interface is equal to zero. In the isotropic and z-transversly isotropic cases, under uniaxial stress, the contraction along the x- and y-directions is equal to one half of the elongation along the z-direction (the theoretical analysis is here carried out using the small-strain framework), and the classical result of $54.74°$ is obtained, cf. Fig. 18a. In the x- and y-transversely isotropic cases, the transformation strain within the band is determined from the stationarity condition (35). Specifically, the transformation strain $\bar{e}^{\mathrm{t}}$ is found such that the uniaxial stress is normal to the surface $g(\bar{e}^{\mathrm{t}}) = 0$. The resulting orientation angle depends then on parameter β, see Fig. 18b. The isotropic case is recovered for $\beta = \alpha$. The inclination angle increases as β decreases in the x-transversely isotropic case, and the trend is opposite in the y-transversely isotropic case. The limiting case of transformation strain vanishing along the x- and y-direction has been examined by Wendler et al. (2017), and the respective inclination angles have been found equal to $90°$ and $45°$, respectively, in agreement with the trends observed in Fig. 18 (note, however, that the limiting cases of Wendler et al. (2017) cannot be achieved in the case of the present model).

In all cases, the finite-element results match well the theoretical predictions. The small systematic deviation visible in Fig. 18 may be caused by the boundary conditions that may induce the stress which is not exactly uniaxial. A significant deviation is only observed in the isotropic and x-transversely isotropic cases when, respectively, α and β are close to 0.7. The isotropic case with α close to 0.7 corresponds to tension–compression asymmetry with the transformation stress in tension higher than that in compression. The transformation (yield) surface in the stress space, which is not available in a closed form, but can be determined numerically, exhibits then a sharp, even if smooth, vertex at the state corresponding to uniaxial tension. Accordingly, a small deviation of the stress tensor from the uniaxial stress may cause a significant change of the transformation strain, which may explain the observed deviation.

The effect of the tension–compression asymmetry and transverse isotropy on the interface thickness has also been examined. This effect has been found negligible.

5. Conclusions

A gradient-enhanced 3D finite-strain model of pseudoelasticity has been developed for the simulation of transformation patterns in polycrystalline shape memory alloys. This has been achieved by enhancing the non-gradient model of pseudoelasticity (Stupkiewicz and Petryk, 2013) following the approach developed recently by Rezaee-Hajidehi and Stupkiewicz (2018). In particular, a micromorphic-type regularization (cf. Mazière and Forest, 2015) has been applied in order to facilitate the finite-element implementation.

The formulation employs the incremental energy minimization framework. In view of the rate-independent dissipation and constitutive inequality constraints, the resulting minimization problem is non-smooth, and the augmented Lagrangian method is used to efficiently handle the related difficulties (cf. Stupkiewicz and Petryk, 2013). Furthermore, thanks to the micromorphic regularization, the non-smooth subproblem is solved locally at the Gauss points, and the non-smoothness does not influence the problem at the global level.

A general thermomechanical formulation has also been developed for the micromorphic model at hand. The general model is thermodynamically consistent and considers all related couplings. In the model actually employed in the finite-element computations, only two most essential couplings are accounted for. Firstly, the latent heat of transformation and the dissipated energy are introduced into the heat conduction equation as a source term. Secondly, the chemical energy is assumed to depend on the resulting local temperature thus influencing the transformation criterion. As illustrated by the NiTi dog-bone example, this suffices to correctly represent the loading-rate effects.

To illustrate the potential of the model, three 3D numerical examples have been analyzed. It has been shown that the model can effectively reproduce complex transformation patterns, including multiple inclined interfaces as well as butterfly-shaped interfaces in a NiTi dog-bone specimen and multi-prong interfaces in a NiTi tube under uniaxial tension. The capability of the model in capturing the major thermomechanical coupling effects has also been illustrated. This, in particular, concerns the effect of the loading rate on the number of martensite bands and the transition from a plateau-type response at low loading rates to an apparent hardening response at higher rates.

A detailed study of the characteristics of the macroscopic transformation front has also been performed for a NiTi strip under uniaxial tension. It has been shown that the inclination angle is influenced by the tension–compression asymmetry and transverse isotropy, however, the effect is not much pronounced in the physically relevant range of the material parameters. On the other hand, these features do not influence the interface thickness, which only depends on the specimen thickness. When the specimen thickness approaches zero, the interface thickness approaches the theoretical thickness that is governed by the softening- and gradient-related parameters in the Helmholtz free energy function.

The focus of this work has been on strain localization, macroscopic transformation fronts, and related phenomena. The monolithic, implicit computational scheme developed has proven effective in simulating relevant 3D boundary value problems and, in particular, in reproducing complex transformation patterns. At the same time, the adopted constitutive description involves some simplifications such as the underlying trilinear pseudoelastic stress–strain response and no dissipation associated with reorientation of martensite. Addressing the related issues will be the topic of our future work.

Appendix A. Local 1D model of pseudoelasticity

A local 1D version of the model presented in Section 2.1 is described here to demonstrate the stress-strain response and the transformation criterion in this simple case. For details, including the gradient-enhanced formulations in 1D, the reader is referred to Rezaee-Hajidehi and Stupkiewicz (2018).

In the 1D small-strain setting, the total strain $\varepsilon = \nabla u$ is additively decomposed into its elastic ε^{e} and transformation ε^{t} parts,

$$\varepsilon = \varepsilon^{\mathrm{e}} + \varepsilon^{\mathrm{t}}, \qquad \varepsilon^{\mathrm{t}} = \eta \epsilon_{\mathrm{T}}, \tag{A.1}$$

where ϵ_{T} is the transformation strain of the fully oriented martensite, and it is here assumed constant. Assuming further that the hardening modulus H is constant, the Helmholtz free energy function (5) simplifies to

$$\phi(\varepsilon, \eta) = \phi_0^{\mathrm{a}} + \Delta \phi_0 \eta + \frac{1}{2} E (\varepsilon - \eta \epsilon_{\mathrm{T}})^2 + \frac{1}{2} H \eta^2, \tag{A.2}$$

where E is the Young's modulus of elasticity which is assumed the same for austenite and martensite. Note that the gradient term ϕ_{grad} is absent in the local model.

Following the general procedure described in Section 2.1, the solution $\{u, \eta\}$ at the current time instant $t = t_{n+1}$ is obtained by minimizing the global incremental potential $\Pi[u, \eta]$ with respect to the fields of u and η,

$$\{u, \eta\} = \arg \min_{u, \eta} \Pi[u, \eta], \qquad \Pi[u, \eta] = \mathcal{E}[u, \eta] - \mathcal{E}[u_n, \eta_n] + \Delta \mathcal{D}[\eta] + \mathcal{I}[\eta]. \tag{A.3}$$

By minimizing $\Pi[u, \eta]$ with respect to the displacement field u, for a fixed field of η, a stable equilibrium is found which, in the absence of body forces, is expressed in the standard form,

$$\nabla \cdot \sigma = 0, \qquad \sigma = E(\varepsilon - \eta \epsilon_{\mathrm{T}}). \tag{A.4}$$

Minimization (A.3) with respect to η can be performed locally (pointwise), thus yielding the volume fraction η as a function of the strain ε. The necessary condition for the minimum can be

written in the form of the following inclusion, cf. Eq. (33),

$$f_\eta \in \partial \bar{D}(\eta), \qquad f_\eta = -\frac{\partial \phi}{\partial \eta} = -\Delta \phi_0 + \sigma \epsilon_{\mathrm{T}} - H\eta, \qquad (\mathrm{A.5})$$

where f_η is the thermodynamic driving force. When the transformation proceeds with $\Delta \eta \neq 0$ and $0 < \eta < 1$, inclusion $(\mathrm{A.5})_1$ gives the following transformation criterion,

$$f = \pm f_c \quad \Leftrightarrow \quad \sigma_\pm^{\mathrm{t}} = \frac{\Delta \phi_0 \pm f_c + H\eta}{\epsilon_{\mathrm{T}}}, \qquad (\mathrm{A.6})$$

where σ_+^{t} (σ_-^{t}) is the transformation stress associated with the forward (reverse) transformation. Eq. (A.6) implies that the hardening/softening behaviour during transformation is controlled by the parameter H, with hardening for $H > 0$ and softening for $H < 0$, cf. Fig. 1(a).

Appendix B. Thermomechanical formulation

Appendix B.1. General framework

In this appendix, a general thermomechanical formulation is developed for the micromorphic model introduced in Section 2.2. In the micromorphic approach, the micromorphic variable $\breve{\eta}$ is treated as an additional internal degree of freedom for which a generalized balance of micromorphic momentum is derived starting from the extended virtual work of internal and external forces. This part is described very briefly below, and, for the details, the reader is referred to Forest (2009). Subsequently, the balance of internal energy is analyzed in detail by following the thermodynamic framework of Rajagopal and Srinivasa (2000), see also Hron et al. (2017), to arrive at the general form of the heat conduction equation that is consistent with the second law of thermodynamics.

With reference to the constitutive framework introduced in Section 2.2, the Helmholtz free energy density ϕ is here assumed to depend on the deformation gradient $\boldsymbol{F} = \nabla \boldsymbol{\varphi}$, temperature T, internal variables $\bar{\boldsymbol{e}}^{\mathrm{t}}$ and η, and also on $\breve{\eta}$, the micromorphic counterpart of η, and its gradient $\nabla \breve{\eta}$, so that $\phi = \phi(\boldsymbol{F}, \bar{\boldsymbol{e}}^{\mathrm{t}}, \eta, \breve{\eta}, \nabla \breve{\eta}, T)$. It is recalled that η and $\bar{\boldsymbol{e}}^{\mathrm{t}}$ are subject to the constitutive constraints $0 \leq \eta \leq 1$ and $g(\bar{\boldsymbol{e}}^{\mathrm{t}}) = 0$, respectively. Apart from that, the form of the free energy function ϕ is here left unspecified. The special case of the constitutive equations introduced in Section 2 is discussed in Appendix B.2. The derivations are here carried out in the referential description so that, in particular, the gradient denoted by ∇ is evaluated in the reference configuration.

Following the micromorphic approach of Forest (2009), the placement $\boldsymbol{\varphi}$ and the micromorphic variable $\breve{\eta}$ are treated as independent degrees of freedom. Accordingly, the extended virtual work (or virtual power) of internal and external (contact) forces, respectively, $\mathcal{P}^{(\mathrm{i})}$ and $\mathcal{P}^{(\mathrm{c})}$, is formulated for any subdomain D of the body B in the following form,

$$\mathcal{P}^{(\mathrm{i})} = \int_D (\boldsymbol{P} \cdot \nabla \delta \boldsymbol{\varphi} + a\, \delta \breve{\eta} + \boldsymbol{b} \cdot \nabla \delta \breve{\eta}) \mathrm{d}V, \qquad \mathcal{P}^{(\mathrm{c})} = -\int_{\partial D} (\boldsymbol{t} \cdot \delta \boldsymbol{\varphi} + a_{\mathrm{c}} \delta \breve{\eta}) \mathrm{d}S, \qquad (\mathrm{B.1})$$

where $\delta\boldsymbol{\varphi}$ and $\delta\breve{\eta}$ are the variations (or virtual velocities) of $\boldsymbol{\varphi}$ and $\breve{\eta}$, respectively, $\boldsymbol{P}$ is the first Piola–Kirchhoff stress tensor, and $\boldsymbol{t}$ is the nominal traction vector. Furthermore, a and $\boldsymbol{b}$ are the generalized stresses associated with the micromorphic variable $\breve{\eta}$ and its first gradient $\nabla\breve{\eta}$, and a_{c} is a generalized traction. For simplicity, body forces and generalized body forces are not considered here. Accordingly, the generalized principle of virtual work reads

$$\mathcal{P}^{(\mathrm{i})} + \mathcal{P}^{(\mathrm{c})} = 0 \qquad \forall\, D,\ \ \forall\, \delta\boldsymbol{\varphi},\ \ \forall\, \delta\breve{\eta}, \tag{B.2}$$

which, upon applying the divergence theorem, yields the standard balance of momentum equation and the generalized balance of micromorphic momentum equation, viz.

$$\nabla \cdot \boldsymbol{P}^{\mathrm{T}} = \boldsymbol{0}, \qquad \nabla \cdot \boldsymbol{b} - a = 0 \qquad \text{in } D, \tag{B.3}$$

as well as the boundary conditions for the standard and generalized tractions,

$$\boldsymbol{t} = \boldsymbol{P}\boldsymbol{\nu}, \qquad a_{\mathrm{c}} = \boldsymbol{b} \cdot \boldsymbol{\nu} \qquad \text{on } \partial D, \tag{B.4}$$

where $\boldsymbol{\nu}$ is the unit outer normal to ∂D.

As the next step, the balance of internal energy is formulated such that it includes the power of the generalized forces a and $\boldsymbol{b}$, cf. Eq. (B.1)$_1$,

$$\varrho_0 \dot{e} = \boldsymbol{P} \cdot \dot{\boldsymbol{F}} + a\,\dot{\breve{\eta}} + \boldsymbol{b} \cdot \nabla\dot{\breve{\eta}} - \nabla \cdot \boldsymbol{Q}, \tag{B.5}$$

where e is the internal energy density per unit mass and $\boldsymbol{Q}$ is the nominal heat flux.

The internal energy e (with the entropy s as an independent variable) and the Helmholtz free energy ϕ (with the temperature T as an independent variable) are related by the following Legendre transformation,

$$\frac{1}{\varrho_0}\phi(\boldsymbol{F}, \bar{\boldsymbol{e}}^{\mathrm{t}}, \eta, \breve{\eta}, \nabla\breve{\eta}, T) = e(\boldsymbol{F}, \bar{\boldsymbol{e}}^{\mathrm{t}}, \eta, \breve{\eta}, \nabla\breve{\eta}, s(\boldsymbol{F}, \bar{\boldsymbol{e}}^{\mathrm{t}}, \eta, \breve{\eta}, \nabla\breve{\eta}, T)) - Ts(\boldsymbol{F}, \bar{\boldsymbol{e}}^{\mathrm{t}}, \eta, \breve{\eta}, \nabla\breve{\eta}, T), \tag{B.6}$$

which implies that

$$s = -\frac{1}{\varrho_0}\frac{\partial\phi}{\partial T}, \tag{B.7}$$

where s is here defined as the density per unit mass. By taking the time derivative of Eq. (B.6) and using Eq. (B.7), the rate of the internal energy e is obtained in the following form,

$$\varrho_0 \dot{e} = \frac{\partial\phi}{\partial \boldsymbol{F}} \cdot \dot{\boldsymbol{F}} + \frac{\partial\phi}{\partial \bar{\boldsymbol{e}}^{\mathrm{t}}} \cdot \dot{\bar{\boldsymbol{e}}}^{\mathrm{t}} + \frac{\partial\phi}{\partial \eta}\dot{\eta} + \frac{\partial\phi}{\partial \breve{\eta}}\dot{\breve{\eta}} + \frac{\partial\phi}{\partial \nabla\breve{\eta}} \cdot \nabla\dot{\breve{\eta}} + \varrho_0 T\dot{s}. \tag{B.8}$$

Upon inserting $\dot{e}$ given by Eq. (B.8) into the internal energy balance (B.5), dividing the resulting equation by T, and using the identity,

$$\nabla \cdot \left(\frac{\boldsymbol{Q}}{T}\right) = \frac{\nabla \cdot \boldsymbol{Q}}{T} - \frac{\boldsymbol{Q} \cdot \nabla T}{T^2}, \tag{B.9}$$

we get

$$\varrho_0 \dot{s} + \nabla \cdot \left(\frac{\boldsymbol{Q}}{T}\right) = \frac{1}{T}\left(\left(\boldsymbol{P} - \frac{\partial\phi}{\partial\boldsymbol{F}}\right)\cdot\dot{\boldsymbol{F}} - \frac{\partial\phi}{\partial\bar{\boldsymbol{e}}^{\mathrm{t}}}\cdot\dot{\bar{\boldsymbol{e}}}^{\mathrm{t}} - \frac{\partial\phi}{\partial\eta}\,\dot{\eta} + \left(a - \frac{\partial\phi}{\partial\breve{\eta}}\right)\dot{\breve{\eta}} + \left(\boldsymbol{b} - \frac{\partial\phi}{\partial\nabla\breve{\eta}}\right)\cdot\nabla\dot{\breve{\eta}} - \boldsymbol{Q}\cdot\frac{\nabla T}{T}\right).$$
(B.10)

Equation (B.10) is recognized as the balance of entropy,

$$\varrho_0 \dot{s} + \nabla \cdot \boldsymbol{j}_s = \xi,$$
(B.11)

where the entropy flux $\boldsymbol{j}_s$ and the entropy production rate ξ are of the form

$$\boldsymbol{j}_s = \frac{\boldsymbol{Q}}{T},$$
(B.12)

and

$$\xi = \frac{1}{T}\left(\left(\boldsymbol{P} - \frac{\partial\phi}{\partial\boldsymbol{F}}\right)\cdot\dot{\boldsymbol{F}} - \frac{\partial\phi}{\partial\bar{\boldsymbol{e}}^{\mathrm{t}}}\cdot\dot{\bar{\boldsymbol{e}}}^{\mathrm{t}} - \frac{\partial\phi}{\partial\eta}\,\dot{\eta} + \left(a - \frac{\partial\phi}{\partial\breve{\eta}}\right)\dot{\breve{\eta}} + \left(\boldsymbol{b} - \frac{\partial\phi}{\partial\nabla\breve{\eta}}\right)\cdot\nabla\dot{\breve{\eta}} - \boldsymbol{Q}\cdot\frac{\nabla T}{T}\right).$$
(B.13)

In order to satisfy the second law of thermodynamics, the entropy production rate ξ must be non-negative. Constitutively, the following entropy production rate $\tilde{\xi}$ is chosen

$$\tilde{\xi} = \frac{1}{T}\left(f_{\mathrm{c}}|\dot{\eta}| + \frac{K\nabla T\cdot\boldsymbol{C}^{-1}\nabla T}{T}\right) \geq 0,$$
(B.14)

which is non-negative because $f_{\mathrm{c}} > 0$, $K > 0$ and $\boldsymbol{C}$ is positive definite. The governing equations are then obtained by requiring that ξ is equal to $\tilde{\xi}$. The specific form of $\tilde{\xi}$ in Eq. (B.14) is, in fact, a constitutive assumption implying that the heat conduction and the phase transformation are the only sources of entropy production, the remaining processes being non-dissipative.

Enforcing $\xi = \tilde{\xi}$ implies that the terms in the parentheses in front of $\dot{\boldsymbol{F}}$, $\dot{\breve{\eta}}$ and $\nabla\dot{\breve{\eta}}$ in Eq. (B.13) must vanish, which yields the following relationships,

$$\boldsymbol{P} = \frac{\partial\phi}{\partial\boldsymbol{F}}, \qquad a = \frac{\partial\phi}{\partial\breve{\eta}}, \qquad \boldsymbol{b} = \frac{\partial\phi}{\partial\nabla\breve{\eta}}.$$
(B.15)

The first relationship delivers the standard constitutive equation, cf. Eq. (38), while the second and the third one define the generalized stresses a and $\boldsymbol{b}$. Substituting a and $\boldsymbol{b}$, Eq. (B.15)$_{2,3}$, in the micromorphic momentum balance equation (B.3)$_2$ yields

$$\frac{\delta\Phi}{\delta\breve{\eta}} = \frac{\partial\phi}{\partial\breve{\eta}} - \nabla\cdot\frac{\partial\phi}{\partial\nabla\breve{\eta}} = 0, \qquad \Phi = \int_B \phi\,\mathrm{d}V,$$
(B.16)

which is recognized as the Euler–Lagrange equation that represents the condition of stationarity of the free energy functional Φ with respect to $\breve{\eta}$. It can be easily checked that, for the constitutive functions specified in Section 2.1.1, Eq. (B.16) particularizes to the Helmholtz-type equation (41).

Furthermore, $\xi = \tilde{\xi}$ implies that the second term on the right-hand side of Eq. (B.13) vanishes, i.e. $\partial\phi/\partial\bar{\boldsymbol{e}}^{\mathrm{t}}\cdot\dot{\bar{\boldsymbol{e}}}^{\mathrm{t}} = 0$. Recall that evolution of $\bar{\boldsymbol{e}}^{\mathrm{t}}$ is constrained by the condition $g(\bar{\boldsymbol{e}}^{\mathrm{t}}) = 0$, and

44

thus the rate $\dot{\bar{e}}^{\mathrm{t}}$ is tangent to the surface $g(\bar{e}^{\mathrm{t}}) = 0$, i.e. $\partial g/\partial \bar{e}^{\mathrm{t}} \cdot \dot{\bar{e}}^{\mathrm{t}} = 0$. It follows that the thermodynamic driving force $\boldsymbol{f}_{\bar{e}^{\mathrm{t}}} = -\partial \phi/\partial \bar{e}^{\mathrm{t}}$, cf. Eq. (36), is normal to the surface $g(\bar{e}^{\mathrm{t}}) = 0$ and hence the necessary condition (35) is implied.

Finally, by equating the terms involving ∇T in ξ and in $\tilde{\xi}$, the Fourier's law is obtained, cf. Eq. $(47)_2$,

$$\boldsymbol{Q} = -K\boldsymbol{C}^{-1}\nabla T. \tag{B.17}$$

Likewise, by equating the terms involving $\dot{\eta}$, the following transformation condition, expressed here in terms of the thermodynamic driving force $f_\eta = -\partial \phi/\partial \eta$, cf. Eq. (34), is obtained,

$$f_\eta = f_{\mathrm{c}} \operatorname{sign} \dot{\eta} \quad \text{if } \dot{\eta} \neq 0, \tag{B.18}$$

which is consistent with the inclusion (33) derived in Section 2.3. If $\dot{\eta} = 0$, which includes the case when the bound constraints $0 \leq \eta \leq 1$ are active, the terms involving $\dot{\eta}$ vanish both in ξ and in $\tilde{\xi}$.

Now, upon substituting Eqs. (B.7), (B.12), (B.14) and (B.17) into Eq. (B.11) and multiplying by T, the following equation is obtained,

$$-T\frac{\mathrm{d}}{\mathrm{d}t}\left(\frac{\partial \phi}{\partial T}\right) - \nabla \cdot (K\boldsymbol{C}^{-1}\nabla T) = f_{\mathrm{c}}|\dot{\eta}|. \tag{B.19}$$

By inserting the time derivative of $\partial \phi/\partial T$, i.e.,

$$\frac{\mathrm{d}}{\mathrm{d}t}\left(\frac{\partial \phi}{\partial T}\right) = \frac{\partial^2 \phi}{\partial T \partial \boldsymbol{F}} \cdot \dot{\boldsymbol{F}} + \frac{\partial^2 \phi}{\partial T \partial \bar{e}^{\mathrm{t}}} \cdot \dot{\bar{e}}^{\mathrm{t}} + \frac{\partial^2 \phi}{\partial T \partial \eta}\dot{\eta} + \frac{\partial^2 \phi}{\partial T \partial \breve{\eta}}\dot{\breve{\eta}} + \frac{\partial^2 \phi}{\partial T \partial \nabla \breve{\eta}} \cdot \nabla \dot{\breve{\eta}} + \frac{\partial^2 \phi}{\partial T^2}\dot{T}, \tag{B.20}$$

into Eq. (B.19), the general form of the heat conduction equation is finally derived,

$$-T\frac{\partial^2 \phi}{\partial T^2}\dot{T} - \nabla \cdot (K\boldsymbol{C}^{-1}\nabla T) = f_{\mathrm{c}}|\dot{\eta}| + T\left(\frac{\partial^2 \phi}{\partial T \partial \boldsymbol{F}} \cdot \dot{\boldsymbol{F}} + \frac{\partial^2 \phi}{\partial T \partial \bar{e}^{\mathrm{t}}} \cdot \dot{\bar{e}}^{\mathrm{t}} + \frac{\partial^2 \phi}{\partial T \partial \eta}\dot{\eta} + \frac{\partial^2 \phi}{\partial T \partial \breve{\eta}}\dot{\breve{\eta}} + \frac{\partial^2 \phi}{\partial T \partial \nabla \breve{\eta}} \cdot \nabla \dot{\breve{\eta}}\right). \tag{B.21}$$

Concluding, the thermodynamic framework presented above delivers all the governing equations of the isothermal model that have been independently derived in Sections 2.2 and 2.3 using the incremental energy minimization approach. Additionally, the general equation of heat conduction (B.21) has been derived, which includes all possible thermomechanical coupling terms (the second term on the right-hand side). Though not explicitly indicated above, the framework admits arbitrary temperature dependence of the material parameters.

Appendix B.2. Specific form of the heat conduction equation

We now assume that the Helmholtz free energy function ϕ is of the following form,

$$\phi(\boldsymbol{F}, \bar{e}^{\mathrm{t}}, \eta, \breve{\eta}, \nabla \breve{\eta}, T) = \phi_0(\eta, T) + \phi_{\mathrm{el}}(\boldsymbol{F}, \bar{e}^{\mathrm{t}}, \eta) + \phi_{\mathrm{int}}(\bar{e}^{\mathrm{t}}, \eta) + \phi_{\mathrm{grad}}^\mu(\eta, \breve{\eta}, \nabla \breve{\eta}), \tag{B.22}$$

so that the chemical energy contribution ϕ_0 depends on the temperature, the remaining contributions being temperature independent, cf. Eq. (26). Substituting the expressions for ϕ_0^{a} and ϕ_0^{m}

provided by Eq. (43) in Eq. (42), the chemical energy contribution ϕ_0 is given by

$$\phi_0(\eta, T) = u_0^{\mathrm{a}} - s_0^{\mathrm{a}}T + \Delta s^*(T - T_{\mathrm{t}})\eta + \varrho_0 \bar{c}\Big(T - T_0 - T \log \frac{T}{T_0}\Big), \tag{B.23}$$

where $\bar{c} = (1 - \eta)c^{\mathrm{a}} + \eta c^{\mathrm{m}}$ is the weighted average of the specific heat capacities c^{a} and c^{m}, and Δs^* and T_{t} are defined in Section 2.4.

Upon substituting Eq. (B.22) in the general heat conduction equation (B.21), the partial derivatives present in Eq. (B.21) are obtained as

$$\frac{\partial^2 \phi}{\partial T^2} = -\frac{\varrho_0 \bar{c}}{T}, \qquad \frac{\partial^2 \phi}{\partial T \partial \eta} = \Delta s^* + \varrho_0(c^{\mathrm{a}} - c^{\mathrm{m}}) \log \frac{T}{T_0}, \tag{B.24}$$

while the other partial derivatives vanish

$$\frac{\partial^2 \phi}{\partial T \partial \boldsymbol{F}} = \boldsymbol{0}, \quad \frac{\partial^2 \phi}{\partial T \partial \bar{\boldsymbol{e}}^{\mathrm{t}}} = \boldsymbol{0}, \quad \frac{\partial^2 \phi}{\partial T \partial \breve{\eta}} = 0, \quad \frac{\partial^2 \phi}{\partial T \partial \nabla \breve{\eta}} = \boldsymbol{0}. \tag{B.25}$$

Assuming further that the heat capacities are equal, thus $c^{\mathrm{a}} = c^{\mathrm{m}} = \bar{c} = c$, Eq. (B.24) simplifies to

$$\frac{\partial^2 \phi}{\partial T} = -\frac{\varrho_0 c}{T}, \qquad \frac{\partial^2 \phi}{\partial T \partial \eta} = \Delta s^*, \tag{B.26}$$

and the general heat conduction equation (B.21) particularizes to the specific form (46) introduced in Section 2.4.

References

Alessi, R., Bernardini, D., 2015. Analysis of localization phenomena in Shape Memory Alloys bars by a variational approach. Int. J. Solids Struct. 73, 113–133.

Armattoe, K.M., Haboussi, M., Ben Zineb, T., 2014. A 2D finite element based on a nonlocal constitutive model describing localization and propagation of phase transformation in shape memory alloy thin structures. Int. J. Solids Struct. 51, 1208–1220.

Auricchio, F., Bonetti, E., Scalet, G., Ubertini, F., 2014. Theoretical and numerical modeling of shape memory alloys accounting for multiple phase transformations and martensite reorientation. Int. J. Plast. 59, 30–54.

Badnava, H., Kadkhodaei, M., Mashayekhi, M., 2014. A non-local implicit gradient-enhanced model for unstable behaviors of pseudoelastic shape memory alloys in tensile loading. Int. J. Solids Struct. 51, 4015–4025.

Badnava, H., Mashayekhi, M., Kadkhodaei, M., Amiri-Rad, A., 2018. A non-local implicit gradient-enhanced model for thermomechanical behavior of shape memory alloys. J. Intel. Mat. Syst. Str. 29, 1818–1834.

Bechle, N.J., Kyriakides, S., 2014. Localization in NiTi tubes under bending. Int. J. Solids Struct. 51, 967–980.

Bechle, N.J., Kyriakides, S., 2016. Evolution of localization in pseudoelastic NiTi tubes under biaxial stress states. Int. J. Plast. 82, 1–31.

Butler, J.F., 1962. Lüders front propagation in low carbon steels. J. Mech. Phys. Solids 10, 313–318.

Chang, B.C., Shaw, J.A., Iadicola, M.A., 2006. Thermodynamics of shape memory alloy wire: modeling, experiments, and application. Continuum Mech. Thermodyn. 18, 83–118.

Churchill, C.B., Shaw, J.A., Iadicola, M.A., 2009. Tips and tricks for characterizing shape memory alloy wire: Part 3—Localization and propagation phenomena. Exp. Tech. 33, 70–78.

Cissé, C., Zaki, W., Ben Zineb, T., 2016. A review of constitutive models and modeling techniques for shape memory alloys. Int. J. Plast. 76, 244–284.

Cissé, C., Zaki, W., Gu, X., Ben Zineb, T., 2017. A nonlinear 3D model for iron-based shape memory alloys considering different thermomechanical properties for austenite and martensite and coupling between transformation and plasticity. Mech. Mater. 107, 1–21.

Dong, L., Zhou, R.H., Wang, X.L., Hu, G.K., Sun, Q.P., 2016. On interfacial energy of macroscopic domains in polycrystalline NiTi shape memory alloys. Int. J. Solids Struct. 80, 445–455.

Duval, A., Haboussi, M., Ben Zineb, T., 2011. Modelling of localization and propagation of phase transformation in superelastic SMA by a gradient nonlocal approach. Int. J. Solids Struct. 48, 1879–1893.

Feng, P., Sun, Q.P., 2006. Experimental investigation on macroscopic domain formation and evolution in polycrystalline NiTi microtubing under mechanical force. J. Mech. Phys. Solids 54, 1568–1603.

Forest, S., 2009. Micromorphic approach for gradient elasticity, viscoplasticity, and damage. J. Eng. Mech. 135, 117–131.

Forest, S., 2016. Nonlinear regularization operators as derived from the micromorphic approach to gradient elasticity, viscoplasticity and damage. Proc. R. Soc. A 472, 20150755.

Geers, M.G.D., Ubachs, R.L.J.M., Engelen, R.A.B., 2003. Strongly non-local gradient-enhanced finite strain elastoplasticity. Int. J. Numer. Meth. Eng. 56, 2039–2068.

Hallai, J.F., Kyriakides, S., 2013. Underlying material response for Lüders-like instabilities. Int. J. Plast. 47, 1–12.

He, Y.J., Sun, Q.P., 2009. Scaling relationship on macroscopic helical domains in NiTi tubes. Int. J. Solids Struct. 46, 4242–4251.

He, Y.J., Sun, Q.P., 2010a. Macroscopic equilibrium domain structure and geometric compatibility in elastic phase transition of thin plates. Int. J. Mech. Sci. 52, 198–211.

He, Y.J., Sun, Q.P., 2010b. Rate-dependent domain spacing in a stretched NiTi strip. Int. J. Solids Struct. 47, 2775–2783.

Helm, D., 2007. Thermomechanics of martensitic phase transitions in shape memory alloys, I. constitutive theories for small and large deformations. J. Mech. Mater. Struct. 2, 87–112.

Hill, R., 1952. On discontinuous plastic states, with special reference to localized necking in thin sheets. J. Mech. Phys. Solids 1, 19–30.

Holzapfel, G.A., 2006. Nonlinear Solid Mechanics. Wiley, Chichester.

Hron, J., Miloš, V., Průša, V., Souček, O., Tůma, K., 2017. On thermodynamics of incompressible viscoelastic rate type fluids with temperature dependent material coefficients. Int. J. Nonlin. Mech. 95, 193–208.

Hudobivnik, B., Korelc, J., 2016. Closed-form representation of matrix functions in the formulation of nonlinear material models. Finite Elem. Anal. Des. 111, 19–32.

Iadicola, M.A., Shaw, J.A., 2004. Rate and thermal sensitivities of unstable transformation behavior in a shape memory alloy. Int. J. Plast. 20, 577–605.

Jiang, D., Kyriakides, S., Bechle, N.J., Landis, C.M., 2017a. Bending of pseudoelastic NiTi tubes. Int. J. Solids Struct. 124, 192–214.

Jiang, D., Kyriakides, S., Landis, C.M., 2017b. Propagation of phase transformation fronts in pseudoelastic NiTi tubes under uniaxial tension. Extreme Mech. Lett. 15, 113–121.

Jiang, D., Kyriakides, S., Landis, C.M., Kazinakis, K., 2017c. Modeling of propagation of phase transformation fronts in NiTi under uniaxial tension. Eur. J. Mech. A–Solids 64, 131–142.

Junker, P., Hackl, K., 2014. A thermo-mechanically coupled field model for shape memory alloys. Continuum Mech. Thermodyn. 26, 859–877.

Kim, K., Daly, S., 2011. Martensite strain memory in the shape memory alloy Nickel-Titanium under mechanical cycling. Exp. Mech. 51, 641–652.

Korelc, J., 2009. Automation of primal and sensitivity analysis of transient coupled problems. Comput. Mech. 44, 631–649.

Korelc, J., Stupkiewicz, S., 2014. Closed-form matrix exponential and its application in finite-strain plasticity. Int. J. Numer. Meth. Eng. 98, 960–987.

Korelc, J., Wriggers, P., 2016. Automation of finite element methods. Springer International Publishing, Switzerland.

Lagoudas, D.C., Entchev, P.B., Popov, P., Patoor, E., Brinson, L.C., Gao, X., 2006. Shape memory alloys, Part II: Modeling of polycrystals. Mech. Mater. 38, 430–462.

León Baldelli, A.A., Maurini, C., Pham, K., 2015. A gradient approach for the macroscopic modeling of superelasticity in softening shape memory alloys. Int. J. Solids Struct. 52, 45–55.

Li, Z.Q., Sun, Q.P., 2002. The initiation and growth of macroscopic martensite band in nano-grained NiTi microtube under tension. Int. J. Plast. 18, 1481–1498.

Mazière, M., Forest, S., 2015. Strain gradient plasticity modeling and finite element simulation of Lüders band formation and propagation. Continuum Mech. Thermodyn. 27, 83–104.

Michaleris, P., Tortorelli, D.A., Vidal, C.A., 1994. Tangent operators and design sensitivity formulations for transient non-linear coupled problems with applications to elastoplasticity. Int. J. Numer. Meth. Eng. 37, 2471–2499.

Miehe, C., 2011. A multi-field incremental variational framework for gradient-extended standard dissipative solids. J. Mech. Phys. Solids 59, 898–923.

Morreau, J., 1974. On unilateral constraints, friction and plasticity, in: Capriz, G., Stampacchia, G. (Eds.), New Variational Techniques in Mathematical Physics. CIME, Edizioni Cremonese, Roma, pp. 175–322.

Nadai, A., 1950. Theory of flow and fracture of solids, Vol. 1, 2nd edition. McGraw-Hill, New York.

Orgéas, L., Favier, D., 1995. Non-symmetric tension-compression behaviour of NiTi alloy. J. Phys. IV 5, 605.

Ortiz, M., Repetto, E.A., 1999. Nonconvex energy minimization and dislocation structures in ductile single crystals. J. Mech. Phys. Solids 47, 397–462.

Patoor, E., Lagoudas, D.C., Entchev, P.B., Brinson, L.C., Gao, X., 2006. Shape memory alloys, Part I: General properties and modeling of single crystals. Mech. Mater. 38, 391–429.

Peerlings, R.H.J., de Borst, R., Brekelmans, W.A.M., de Vree, J.H.P., 1996. Gradient enhanced damage for quasi-brittle materials. Int. J. Numer. Meth. Eng. 39, 3391–3403.

Petryk, H., 2003. Incremental energy minimization in dissipative solids. C. R. Mecanique 331, 469–474.

Pieczyska, E.A., Gadaj, S.P., Nowacki, W.K., Tobushi, H., 2006. Phase-transformation fronts evolution for stress-and strain-controlled tension tests in TiNi shape memory alloy. Exp. Mech. 46, 531–542.

Qiao, L., Rimoli, J.J., Chen, Y., Schuh, C.A.S., Radovitzky, R., 2011. Nonlocal superelastic model of size-dependent hardening and dissipation in single crystal Cu-Al-Ni shape memory alloys. Phys. Rev. Lett. 106, 085504.

Rajagopal, K.R., Srinivasa, A.R., 2000. A thermodynamic frame work for rate type fluid models. J. Non-Newton. Fluid 88, 207–227.

Raniecki, B., Lexcellent, C., Tanaka, K., 1992. Thermodynamic models of pseudoelastic behaviour of shape memory alloys. Arch. Mech. 44, 261–284.

Reedlunn, B., Churchill, C.B., Nelson, E.E., Shaw, J.A., Daly, S.H., 2014. Tension, compression, and bending of superelastic shape memory alloy tubes. J. Mech. Phys. Solids 63, 506–537.

Ren, X., Truskinovsky, L., 2000. Finite scale microstructures in nonlocal elasticity. J. Elasticity 59, 319–355.

Rezaee-Hajidehi, M., Stupkiewicz, S., 2018. Gradient-enhanced model and its micromorphic regularization for simulation of Lüders-like bands in shape memory alloys. Int. J. Solids Struct. 135, 208–218.

Rockafellar, R.T., 1970. Convex Analysis. Princeton University Press, Princeton, New Jersey.

Sadjadpour, A., Bhattacharya, K., 2007. A micromechanics-inspired constitutive model for shape-memory alloys. Smart Mater. Struct. 16, 1751.

Sedmák, P., Pilch, J., Heller, L., Kopeček, J., Wright, J., Sedlák, P., Frost, M., Šittner, P., 2016. Grain-resolved analysis of localized deformation in nickel-titanium wire under tensile load. Science 353, 559–562.

Shaw, J.A., 2000. Simulations of localized thermo-mechanical behavior in a NiTi shape memory alloy. Int. J. Plast. 16, 541–562.

Shaw, J.A., Kyriakides, S., 1997. On the nucleation and propagation of phase transformation fronts in a NiTi alloy. Act. Mater. 45, 683–700.

Stupkiewicz, S., Petryk, H., 2013. A robust model of pseudoelasticity in shape memory alloys. Int. J. Numer. Meth. Eng. 93, 747–769.

Sun, Q.P., Li, Z.Q., 2002. Phase transformation in superelastic NiTi polycrystalline micro-tubes under tension and torsion—from localization to homogeneous deformation. Int. J. Solids Struct. 39, 3797–3809.

Tůma, K., Stupkiewicz, S., Petryk, H., 2018. Rate-independent dissipation in phase-field modelling of displacive transformations. J. Mech. Phys. Solids 114, 117–142.

Wendler, F., Ossmer, H., Chluba, C., Quandt, E., Kohl, M., 2017. Mesoscale simulation of elastocaloric cooling in SMA films. Acta Mater. 136, 105–117.

Zhang, X., Feng, P., He, Y., Yu, T., Sun, Q.P., 2010. Experimental study on rate dependence of macroscopic domain and stress hysteresis in NiTi shape memory alloy strips. Int. J. Mech. Sci. 52, 1660–1670.